Winter 12-15-2018

Radiolabeled Nanohydroxyapatite as a Platform for the Development of New PET Imaging Agents

Stacy Lee Queern
Washington University in St. Louis

WASHINGTON UNIVERSITY IN ST. LOUIS

Department of Chemistry

Dissertation Examination Committee:
Suzanne E. Lapi, Co-Chair
Kevin Moeller, Co-Chair
John R. Bleeke
Buck Rogers
Lee G. Sobotka

Radiolabeled Nanohydroxyapatite as a Platform for the Development of New PET Imaging Agents

by

Stacy L. Queern

A dissertation presented to
The Graduate School
of Washington University in
partial fulfillment of the
requirements for the degree
of Doctor of Philosophy

December 2018
St. Louis, Missouri

Table of Contents

List of Figures

List of Tables

Acknowledgments

I would like to thank Dr. Suzanne E. Lapi for mentoring and continuously encouraging me, providing the opportunity of a diverse network to showcase my research, and taking time to prepare me for my defense. I would like to thank Dr. Lee G. Sobotka and Dr. Kevin Moeller for being on my annual committee and for providing advice and guidance that has continually improved my work and confidence. I would also like to thank Dr. John Bleeke and Dr. Buck Rogers for being part of my defense committee.

In addition, I would like to thank the entire Lapi lab for all their help and support over the last five years. I would especially like to thank Dr. Lauren Radford, Dr. Jennifer Burkemper, Dr. Tolulope Aweda, and Dr. Adriana Massicano for all their advice and support, not only as lab mates but also friends. I would further like to thank Ashlea Franco, group administrator and friend, who helped stock all supplies necessary for my experiments and for always lending an ear when I needed to talk things through. I would like to thank Dr. Norio Yasui for his technical support with the QTOF. I would also like to thank Dr. Tolulope Aweda, Dr. Adriana Massicano, Nicholas Clanton and Solana Fernandez for their guidance and assistance with cell and animal studies.

I would also like to thank those whom I have worked with in collaborative projects: Dr. Heather Hennkens and Dr. Alan Ketring from MURR, Dr. Jonathan Fitzsimmons, Dr. Dmitri Medvedev, and Dr. Cathy Cutler from BNL, and Dr. Amanda Eckermann from Hope College. Their contributions to my understanding of processes involved in this research was a vital part to how much I have grown these past few years.

Lastly, I would like to thank my husband and best supporter, Tim Queern, and my children Maverick and Ryker Queern. Without their support, constant encouragement, and unwavering belief in me, I would have never made it this far.

Stacy L. Queern

Washington University in St. Louis

December 2018

ABSTRACT OF THE DISSERTATION

Radiolabeled nanohydroxyapatite as a platform for the development of new PET imaging agents

by

Stacy L. Queern

Doctor of Philosophy in Chemistry

Washington University in St. Louis, 2018

Dr. Suzanne E. Lapi, Co-Chair

Dr. Kevin Moeller, Co-Chair

Positron emission tomography (PET) imaging utilizes drugs labeled with positron emitters to target and evaluate different biological processes occurring in the body. Tailoring medicine to the individual allows for higher quality of care with better diagnosis and treatment and is a key purpose for advancing research into developing new platforms for PET imaging agents. A PET nuclide of high interest for the development of these agents is ^{89}Zr. This can be attributed to the long half-life of 3.27 days and low positron energy of ^{89}Zr.

In this work, we developed a production method for ^{89}Zr using Y sputtered coins that is now in current use at the University of Alabama at Birmingham for both research and human-use studies. An alternative means of separation for ^{89}Zr from Y using IDA as an eluant with inorganic resin obtained from Brookhaven National Laboratory was also investigated in order to develop a method that alleviated the necessity to remove the chelator before human injections. The low-level activity separations were reproducible with successful test labeling showing the potential this method has as an alternative separation method.

Although ^{89}Zr has great potential as PET nuclide, it is a known bone seeker, meaning if it decomplexes from a chelator, it will be taken up in the bone. The natural affinity of ^{89}Zr for bone can be exploited as a radiolabeling technique using nHAp. Nanoparticles composed of the main component in the bone matrix, nHAp, were used to exploit the natural affinity of ^{89}Zr and other bone-seekers have for bone to develop a platform for PET imaging agents. The particles were easily labeled with high stability and little bone uptake in vivo. As a proof of concept that this could be used to develop targeted imaging agents, co-precipitated nHAp was rapidly modified with an analog of TOC to target SSTR2 receptors in AR42J cells to show specific targeting. Both the cells studies and the preliminary animal studies showed that there was specific targeting of the novel agents. Overall, the preliminary studies with ^{89}Zr-nHAp-phospha-TOC are very promising for nHAp as a new platform for PET imaging agents.

Chapter 1

Introduction

1.1 Nuclear Chemistry

There are several types of radioactive decay, which essentially result in a loss of energy from the nucleus of an atom. The important decay pathways for this work include beta decay and gamma decay. The nuclear equations and a schematic for each type of decay are shown in Figure 1-1. Beta decay consists of three different modes: negative electron emission (β^-), positron emission (β^+), and electron capture (ε). In beta decay, the emitted particle energies have a continuous distribution with a maximum energy of E_{max} where E_{max} is the difference in the initial and final energies of the nuclear state with a subtraction due to the small recoil correction from the daughter nuclide [1-2]. For all nuclear reactions, the change in energy between the initial and final states is referred to as the Q-value.

Type of Decay	Nuclear Equation	Schematic
β^-	${}^{A}_{Z}X \longrightarrow {}^{A}_{Z+1}Y + \beta^- + \bar{\nu} + (\gamma\ rays)$	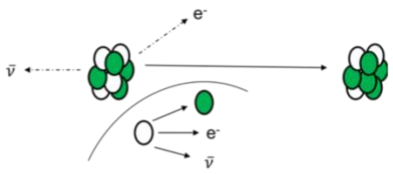
β^+	${}^{A}_{Z}X \longrightarrow {}^{A}_{Z-1}Y + \beta^+ + \nu + (\gamma\ rays)$	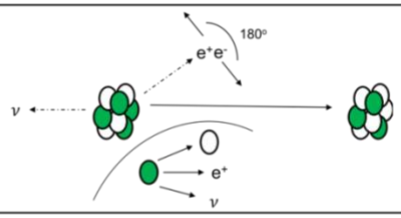
ε	${}^{A}_{Z}X \longrightarrow {}^{A}_{Z-1}Y + {}^{X\text{-}rays\ or}_{Auger\ e^-} + \nu + (\gamma\ rays)$	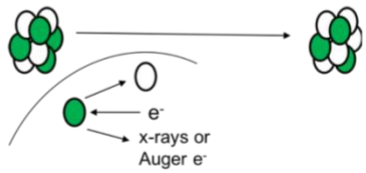
γ	${}^{A}_{Z}X^* \longrightarrow {}^{A}_{Z}X + (\gamma\ rays)$	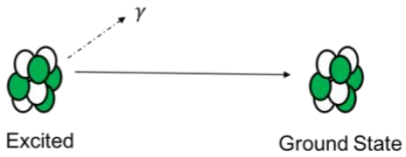

Figure 1-1 Radioactive decay modes

Nuclides that are neutron rich will have a high probability of undergoing β^- decay. In β^- decay, the nucleus of a neutron rich nuclide emits an antineutrino ($\bar{\nu}$) and an electron. This can be thought of as converting a neutron into a proton and increases the value of the atomic number (Z) by one while decreasing the number of neutrons (N) by one. This results in the overall mass number (A) remaining the same [1-2]. Generally, nuclides that undergo β^- decay with half-lives amenable to clinical use can be used to develop radiotherapeutics to help treat disease [3-5]. A relevant medical isotope that undergoes β^- decay is ^{153}Sm with a half-life of 46.5 hours [6].

Nuclides that are proton rich may undergo β^+ or ε decay. In β^+ decay, the nucleus emits a neutrino (ν) and a positron, effectively converting a proton into a neutron. The ejected positron

will annihilate with an electron emitting two photons in opposite directions (approximately 180^{o}) to each other. This type of decay occurs more frequently with lighter nuclei and requires a difference in a mass of the parent and daughter (or Q-value) of greater than 1.02 MeV, the mass of two electrons. For heavier nuclei and for nuclides with a Q-value lower than 1.02 MeV, ε decay is a more probable route of decay. During electron capture, the nucleus captures an orbiting electron effectively converting a proton into a neutron. During ε, there are emissions of x-rays and/or Auger electrons. Auger electrons are low energy electrons emitted from the outer shells of an atom. In both β^+ and ε decay, the value of Z decreases by one while N increases by one to maintain a constant A for the parent and daughter nuclide [1-2]. A parent nuclide may decay by multiple routes (each with a different probability) when there is more than one route available. This is known branching decay. Branching decay of β^+ and ε decay is seen in the decay of ^{55}Co where β^+ decay occurs 77% of the time while ε decay occurs 23% of the time [7-9].

Nuclides that experience beta decay can result in a daughter nuclide in an excited (or metastable) state. This daughter nuclide emits photons or electrons to deexcite to ground state. This decay is known as gamma decay or internal conversion, respectively. An example of this decay is the decay from ^{89m}Zr to ^{89g}Zr. ^{89m}Zr has a half-life of 4.16 minutes with a 94% branching ratio for internal conversion. An example of a decay scheme for ^{89m}Zr to ^{89g}Zr and ^{89}Y is shown Figure 1-2 [7].

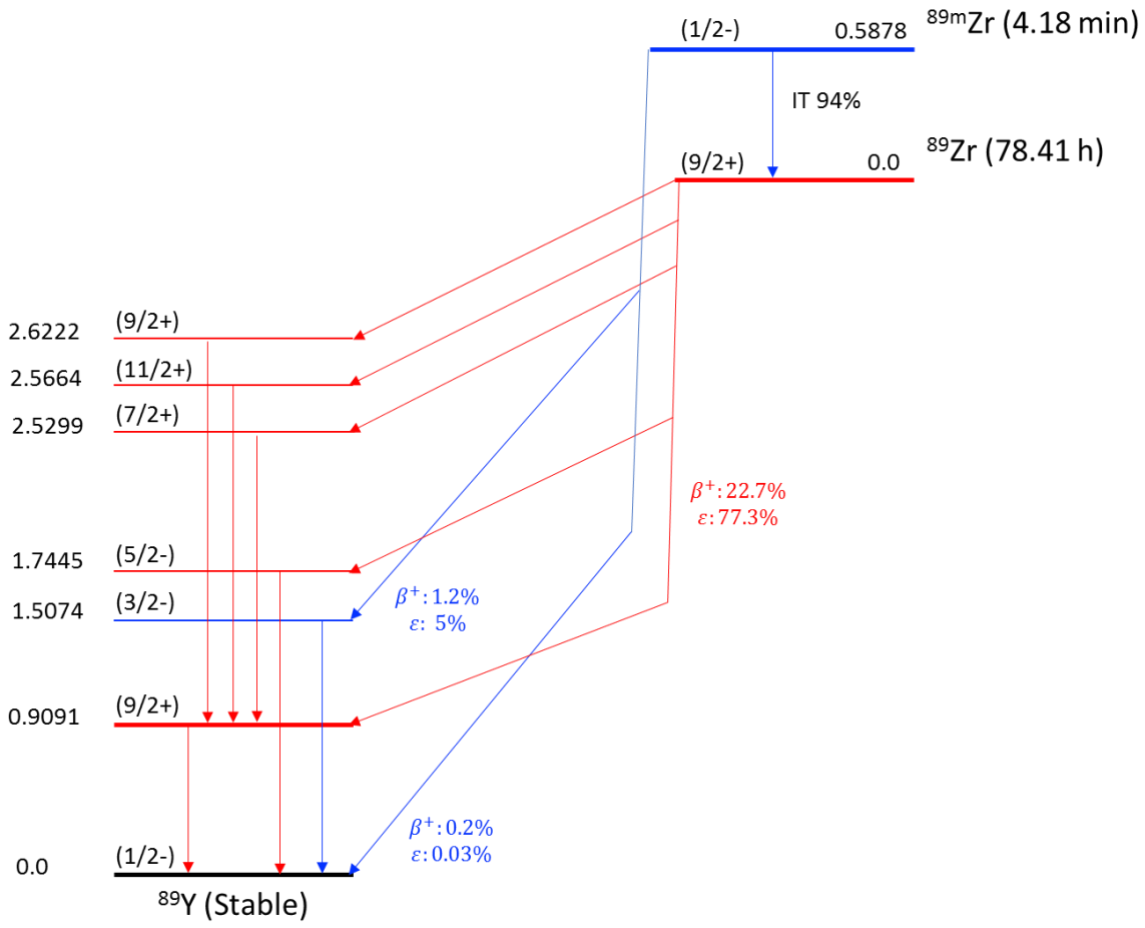

Figure 1-2 Decay scheme for ^{89m}Zr

There are several methods to produce radionuclides for research or clinical activities. In this work, the majority of the radionuclides used were produced using a cyclotron. A cyclotron is a particle accelerator that accelerates charged particles such as protons in a circular path. The ion source releases ions in between two electrodes, often referred to as "dees" for their shape historically. The two dees, where the particles travel, are hollow and shield them from the electric field. Once the particle exits one dee, there is a gap the particle crosses to enter the second dee. In this gap, the electric field will act on the particle accelerating it across and into the opposite dee. To constrain the particles to circular path, the dees are located in a static magnetic field perpendicular to the electric field [1, 8, 10]. As the particles accelerate, the radius of the

path increases until they reach a desired radius/energy. For negative ion accelerators, the extraction port provides a change to the path of negative particles by using extraction foil to strip off electrons. The loss of electrons changes the charge of the ions allowing them to exit the cyclotron into the target material to induce a nuclear reaction [8]. A schematic of a cyclotron is given in Figure 1-3 [1, 8].

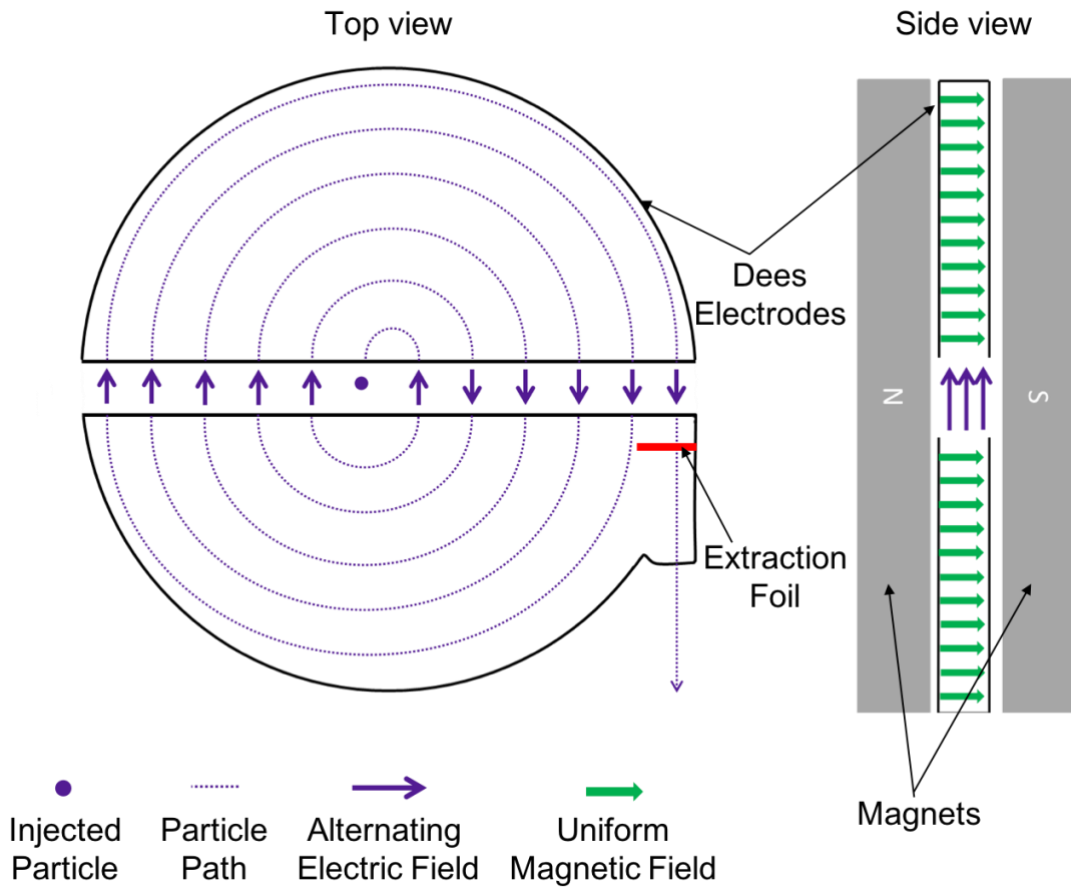

Figure 1-3 Cyclotron schematic

For the production of radionuclides in this work, the main nuclear reactions occur when the nucleus of the target material gains a proton and releases a neutron or alpha particle to obtain the radionuclide of interest. The relevant isotopes are listed in the Table 1-1 [5, 7, 9, 11].

Table 1-1 Relevant radionuclides, production routes, and decay characteristics

Radionuclide	Half-life (h)	Production Route	Decay Routes	$E_{\beta+max}$ (keV)
^{89}Zr	78.41	$^{89}Y(p,n)^{89}Zr$	β^+ (23%) ε (77%)	897
^{18}F	1.83	$^{18}O(p,n)^{18}F$	β^+ (96.7%) ε (3.3%)	635
^{153}Sm	46.5	$^{152}Sm(n,\gamma)^{153}Sm$	β^- (100%)	805 (β^-)
^{64}Cu	12.7	$^{64}Ni(p,n)^{64}Cu$	β^+ (17.6%) ε (43.9%) β^- (38.5%)	653 579 (β^-)
^{55}Co	17.53	$^{58}Ni(p,\alpha)^{55}Co$	β^+ (77%) ε (23%)	1500

The energy of the accelerated particle plays a significant role in the production of these nuclides. A minimum threshold energy is required to induce a nuclear reaction and produce any radionuclide [1, 10]. Once the threshold energy is overcome, the probability of the reaction occurring (cross-section) may be considered [2, 10]. The cross-section plotted against the energy of the projectile is called an excitation function [10, 12]. The excitation function helps determine the range of energies optimal for the production of the radionuclide of interest. An example of an excitation function for the $^{89}Y(p,n)^{89}Zr$ reaction is shown in Figure 1-4 [7, 13].

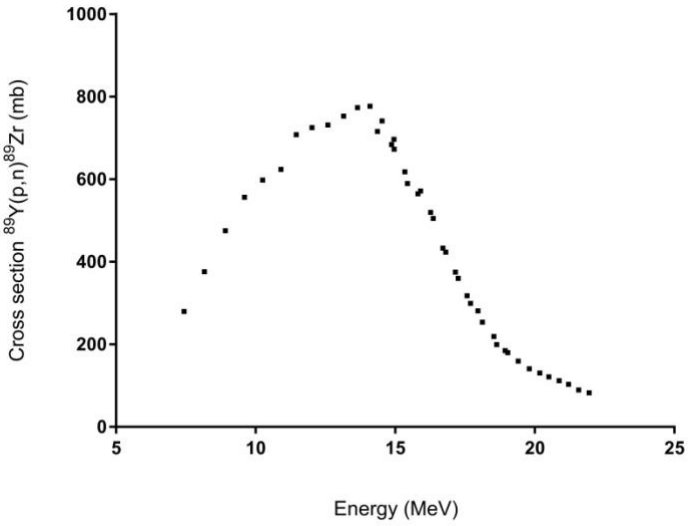

Figure 1-4 Experimental excitation function for ^{89}Y(p,n)^{89}Zr [7, 13]

1.2 Nuclear Medicine

The use of small amounts of radioactivity for diagnosis and treatment of disease is collectively referred to as nuclear medicine. One major tool in nuclear medicine is positron emission tomography (PET) imaging. PET imaging is a noninvasive and quantitative imaging technique that allows for research, diagnosis of disease and development of effective treatment plans.

PET is based on the principle that once a PET nuclide is administered, the nucleus emits a positron and approximately 1 - 10 mm from the emission site, this positron annihilates with an electron to produce two 511 keV photons moving in essentially opposite directions [10]. These photons are detected in coincidence at 180^{o} using scintillation detectors that surround the subject (see Figure 1-5). The images are then reconstructed using each event that is detected in coincidence. One key factor in the resolution of a PET image is the energy of the emitted positron. The maximum positron energy, $E_{\beta+max}$, is a limiting factor for image resolution because

higher energy positrons will propagate through tissue much further then lower energy positrons before the annihilation event occurs [12].

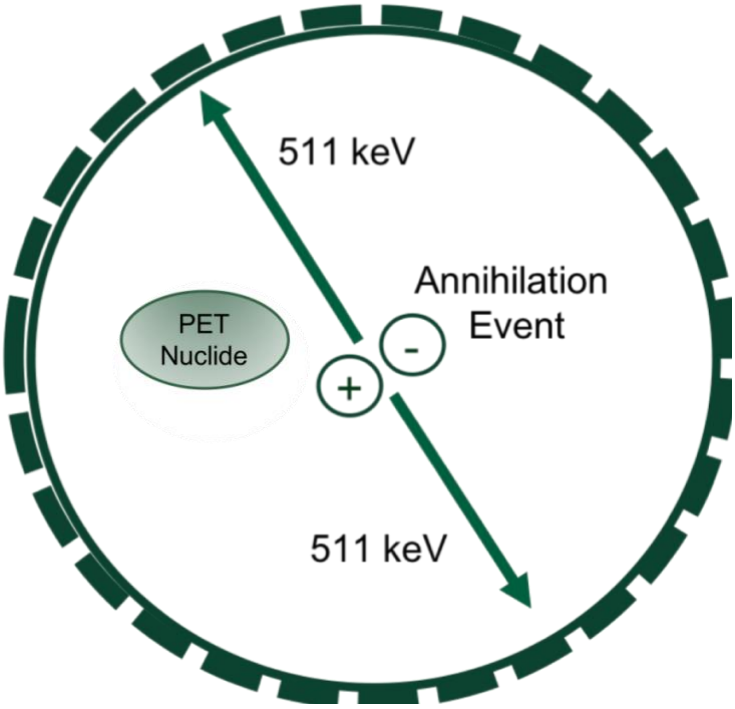

Figure 1-5 PET scanner schematic

The most commonly used PET nuclide is ^{18}F which has an $E_{\beta+max}$ of 635 keV and a half-life of 109.8 minutes [14-15]. Additionally, there are many other PET nuclides currently in use. Table 1-1 shows the common PET nuclides found in this work and their characteristics.

When PET nuclides are utilized in compounds, they are known as PET tracers or radiopharmaceuticals. Most of the time PET tracers are PET nuclides tethered to a targeting agent that delivers the PET nuclide to the intended area (see Figure 1-6). Ideal candidates for PET nuclides would have low $E_{\beta+max}$ and a half-life that matches the biological half-life of agent being studied. All PET tracers should have a relatively short half-life to minimize the radiation exposure to the subject, they should be easily modified and stable, and have a high specific

activity. Specific activity is a measure of radioactivity per total mass and is generally expressed as the amount of radioactivity per mole of compound [1, 8, 12]. Compounds with high specific activity allow for less mass to be used in the dose administered to the patient. This is particularly important when targeting receptors in low abundance or when using pharmacologically active compounds as imaging agents. While there are currently several PET tracers used clinically, the most commonly used PET tracer is 2-[^{18}F]fluoro-2-deoxyglucose ([^{18}F]FDG) which is used for measuring metabolic activity for diagnosis of cancer and other disease states [8, 16-17]. Occasionally, PET nuclides can be injected without being tethered to a targeting agent when the nuclide has a natural high affinity for the intended area. For example, ^{18}F (as F^-) has a natural affinity for bone and is used in bone imaging studies [18-19]. There are a few radionuclides that are bone-seekers with a naturally high affinity for bone, such as ^{89}Zr, ^{18}F, and ^{153}Sm.

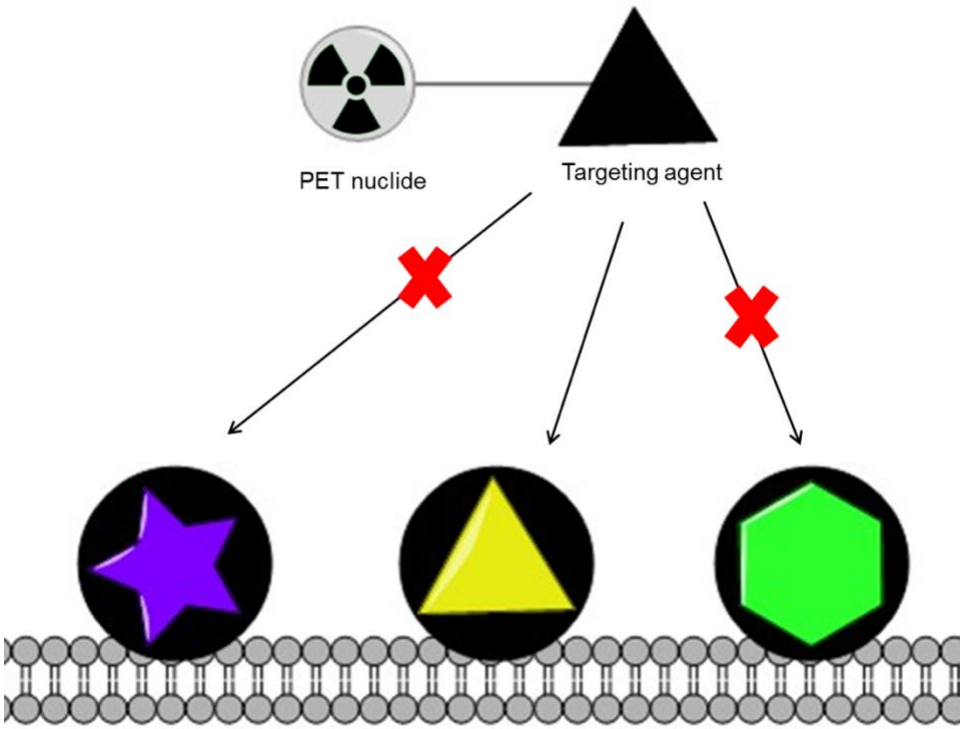

Figure 1-6 PET tracers and targeting mechanisms

The development of PET tracers utilizing ^{89}Zr has been of high interest due to its half-life of 3.27 days [20-21]. This long half-life relative to ^{18}F (109.77 min) is compatible with the biological half-life of antibodies providing longer imaging time points for PET [20, 22-23]. The β^+ branching ratio for ^{89}Zr is 23% and offers high resolution images and quantitative imaging with a maximum positron energy of 0.897 MeV [21-22]. Although ^{89}Zr has great potential as PET nuclide, it is a known bone seeker [23-24]. Thus, if the ^{89}Zr complex is not stable in vivo and the ^{89}Zr decomplexes, it's affinity to bone may cause unnecessary dose for the patient.

In this work, methods for production of ^{89}Zr using both organic and inorganic resins for purification were developed and are discussed in chapters 2 and 3, respectively. Chapter 4 investigates the radiolabeling of nanohydroxyapatite (nHAp), the main component in bone matrix, as a new platform for PET imaging agents. Both known bone-seekers, ^{89}Zr, ^{18}F and ^{153}Sm, and non-bone-seekers, ^{64}Cu and ^{55}Co, were investigated to compare the labeling and stability of radiolabeled nHAp. Two different morphologies of nHAp, sphere and needle, were compared to determine the impact of the shape on the biological properties. Chapter 5 covers an alternative co-precipitation method of nHAp, radiolabeling and modification with the peptide based phosopha-TOC to target SSTR2 receptors which are overexpressed on neuroendocrine tumors. These particles were employed in cell studies using the AR42J cell line to show specific targeting. Rat pancreatic tumors were implanted in immunodeficient mice to assess the in vivo targeting properties of ^{89}Zr-nHAp-phospha-TOC. In chapter 6, conclusions and thoughts for future work are provided. Overall, the goal of this work was to implement nHAp as a new platform for PET imaging agents using ^{89}Zr-nHAp-phospha-TOC as a proof of concept.

1.3 References

1. Ehmann, W. D.; Vance, D. E., *Radiochemistry and nuclear methods of analysis*. Wiley: New York, 1991; p xviii, 531 p.
2. Friedlander, G.; Friedlander, G., *Nuclear and radiochemistry*. 3rd ed.; Wiley: New York, 1981; p xiii, 684 p.
3. Mastren, T.; Pen, A.; Loveless, S.; Marquez, B. V.; Bollinger, E.; Marois, B.; Hubley, N.; Brown, K.; Morrissey, D. J.; Peaslee, G. F.; Lapi, S. E., Harvesting (67)Cu from the Collection of a Secondary Beam Cocktail at the National Superconducting Cyclotron Laboratory. *Anal Chem* **2015,** *87* (20), 10323-9.
4. Rotsch, D. A.; Brown, M. A.; Nolen, J. A.; Brossard, T.; Henning, W. F.; Chemerisov, S. D.; Gromov, R. G.; Greene, J., Electron linear accelerator production and purification of scandium-47 from titanium dioxide targets. *Appl Radiat Isot* **2018,** *131*, 77-82.
5. Cutler, C. S.; Hennkens, H. M.; Sisay, N.; Huclier-Markai, S.; Jurisson, S. S., Radiometals for combined imaging and therapy. *Chem Rev* **2013,** *113* (2), 858-83.
6. Malkowski, B.; Maruszak, M.; Dudek, A.; Wedrowski, M.; Szefer, J., The influence of Sm-153 therapy on bone marrow function. *Contemp Oncol (Pozn)* **2016,** *20* (5), 385-388.
7. National Nuclear Data Center (nndc). http://www.nndc.bnl.gov/exfor/exfor.htm (accessed 25 October).
8. Welch, M. J.; Redvanly, C. S., *Handbook of radiopharmaceuticals : radiochemistry and applications*. J. Wiley: New York, 2003; p xiv, 848 p.
9. Li, Z.; Conti, P. S., Radiopharmaceutical chemistry for positron emission tomography. *Adv Drug Deliv Rev* **2010,** *62* (11), 1031-51.
10. Loveland, W. D.; Morrissey, D. J.; Seaborg, G. T., *Modern nuclear chemistry*. Second edition. ed.; Wiley: Hoboken, NJ, USA, 2017; p xviii, 744 pages.
11. Mastren, T.; Marquez, B. V.; Sultan, D. E.; Bollinger, E.; Eisenbeis, P.; Voller, T.; Lapi, S. E., Cyclotron Production of High-Specific Activity 55Co and In Vivo Evaluation of the Stability of 55Co Metal-Chelate-Peptide Complexes. *Mol Imaging* **2015,** *14* (10), 526-33.
12. Choppin, G. R.; Choppin, G. R.; Liljenzin, J.-O.; Rydberg, J., *Radiochemistry and nuclear chemistry*. 3rd ed.; Butterworth-Heinemann: Woburn, MA, 2002; p 709 p.
13. Mustafa, M. G.; West, H. I., Jr.; O'Brien, H.; Lanier, R. G.; Benhamou, M.; Tamura, T., Measurements and a direct-reaction-plus-Hauser-Feshbach analysis of 89Y(p,n)89Zr, 89Y(p,2n)88, and 89Y(p,pn)88Y reactions up to 40 MeV. *Phys Rev C Nucl Phys* **1988,** *38* (4), 1624-1637.
14. Cole, E. L.; Stewart, M. N.; Littich, R.; Hoareau, R.; Scott, P. J., Radiosyntheses using fluorine-18: the art and science of late stage fluorination. *Curr Top Med Chem* **2014,** *14* (7), 875-900.
15. Coenen, H. H.; Elsinga, P. H.; Iwata, R.; Kilbourn, M. R.; Pillai, M. R.; Rajan, M. G.; Wagner, H. N., Jr.; Zaknun, J. J., Fluorine-18 radiopharmaceuticals beyond [18F]FDG for use in oncology and neurosciences. *Nucl Med Biol* **2010,** *37* (7), 727-40.
16. Alauddin, M. M., Positron emission tomography (PET) imaging with (18)F-based radiotracers. *Am J Nucl Med Mol Imaging* **2012,** *2* (1), 55-76.
17. Brasse, D.; Nonat, A., Radiometals: towards a new success story in nuclear imaging? *Dalton Trans* **2015,** *44* (11), 4845-58.

18. Ulmert, D.; Solnes, L.; Thorek, D., Contemporary approaches for imaging skeletal metastasis. *Bone Res* **2015,** *3*, 15024.
19. Sterner, T.; Pink, R.; Freudenberg, L.; Jentzen, T.; Quitmann, H.; Bockisch, A.; Loer, F., The role of [18F]fluoride positron emission tomography in the early detection of aseptic loosening of total knee arthroplasty. *Int J Surg* **2007,** *5* (2), 99-104.
20. Marquez, B. V.; Ikotun, O. F.; Zheleznyak, A.; Wright, B.; Hari-Raj, A.; Pierce, R. A.; Lapi, S. E., Evaluation of (89)Zr-pertuzumab in Breast cancer xenografts. *Mol Pharm* **2014,** *11* (11), 3988-95.
21. Wooten, A. L. M., E.; Schweitzer, G. D.; Lawrence, L. A.; Mebrahtu, E.; Lewis, B. C.; Lapi, S. E., Routine Production of ^{89}Zr Using Automated Module. *Appl. Sci.* **2013,** *3*, 593-613.
22. Holland, J. P.; Sheh, Y.; Lewis, J. S., Standardized methods for the production of high specific-activity zirconium-89. *Nucl Med Biol* **2009,** *36* (7), 729-39.
23. Deri, M. A.; Zeglis, B. M.; Francesconi, L. C.; Lewis, J. S., PET imaging with (8)(9)Zr: from radiochemistry to the clinic. *Nucl Med Biol* **2013,** *40* (1), 3-14.
24. Abou, D. S.; Ku, T.; Smith-Jones, P. M., In vivo biodistribution and accumulation of (89)Zr in mice. *Nucl Med Biol* **2011,** *38* (5), 675-81.

Chapter 2

Production of ^{89}Zr using sputtered yttrium coin targets

[This work has been published previously as "Production of ^{89}Zr using sputtered yttrium coin targets," Stacy L Queern, Tolulope A. Aweda, Adriana V. F. Massicano, Nicholas A. Clanton, Retta El Sayed, Jayden A. Sader, Alexander Zyuzin, and Suzanne E. Lapi, *Nuclear Medicine and Biology*. **2017**, 50, 11-16]

2.1 Introduction

Radionuclides for radiotracers used in medical imaging can be produced on an accelerator or in a nuclear reactor. A cyclotron is a type of accelerator which offers many advantages for the production of these radionuclides. A medical cyclotron is generally smaller than a linear accelerator, making it more feasible to have on sites with size constraints such as hospitals and universities. Furthermore, the use of a proton accelerating cyclotron (as opposed to a reactor) typically provides products of a different element than the initial target material, allowing for chemical separations leading to a product with high specific activity. Cyclotrons also allow for the production of radionuclides with low impurities through selection of the proper target material and energy range for the protons used in the nuclear reaction. Regarding the production of the radionuclides using a cyclotron, there are two properties of the beam that need to be taken into consideration. The energy of the protons needs to be high enough for the nuclear reaction to occur while remaining in the range of energies to minimize the amount of impurities being produced where possible. Additionally, the beam current will impact the amount of activity being produced. The current needs to be high enough to provide suitable amounts of radioactivity without significantly damaging the target material due to the heat deposited from the beam.

There has been an increasing interest in the production of ^{89}Zr, mainly due to the ^{89}Zr half-life which is compatible with antibody imaging [1-4]. Additional characteristics of this isotope include the ability to carry out high resolution and quantitative imaging due to the branching ratio for β^+ emission (23%) and low average positron energy (396 keV) [1, 3, 5]. While ^{89}Zr also emits a γ-ray at 909 keV at a branching ratio of 99% which is suboptimal for dosimetry, the

longer half-life of ^{89}Zr (3.27 days) relative to the short half-life of commonly used ^{18}F (1.83 hours) has propelled its demand in nuclear medicine for positron emission tomography (PET) for the development of imaging agents requiring longer imaging time points [5-7].

The current method of production for ^{89}Zr is typically via cyclotron or linear accelerator using natural abundance yttrium via the ^{89}Y(p,n)^{89}Zr reaction. Several different types of target material have been investigated including yttrium foil, yttrium oxide powder, yttrium sputtered onto copper, electrodeposition of yttrium, and aqueous yttrium nitrate [1, 3, 8-11]. While there are several reports investigating and optimizing foil, powder and solution targets, there are few reports using sputtered yttrium.

By examining the cross-sections for the production of ^{89}Zr and ^{88}Zr, theoretical calculations of activity and beam energy optimization can be determined [12-13]. Figure 2-1 shows the production of ^{89}Zr via the ^{89}Y(p,n)^{89}Zr reaction is optimal at low proton beam energy (<13 MeV) while at higher beam energy, ^{88}Zr as a contaminant is introduced via the ^{89}Y(p,2n)^{88}Zr reaction [14-15]. While the co-production of ^{89}Zr and ^{88}Zr is inevitable at higher energies, the production of ^{88}Zr can be eliminated by using a lower proton beam energy of <13 MeV [7].

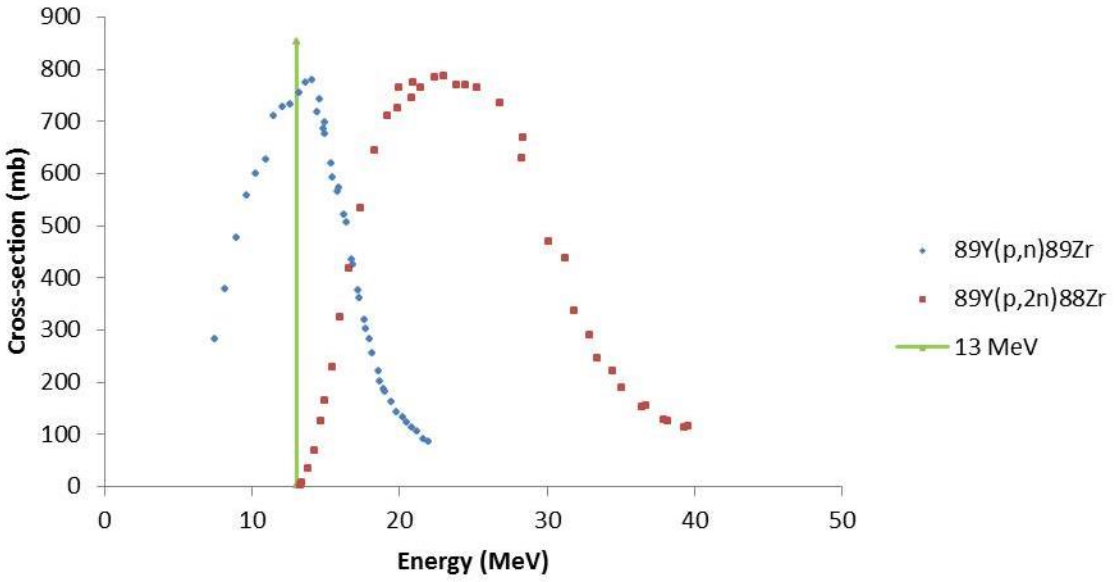

Figure 2-1 Cross-section comparison of ^{89}Y(p,n)^{89}Zr and ^{89}Y(p,2n)^{88}Zr [14-15]

While several ^{89}Zr purification methods have been reported, including solvent exchange, anion exchange, or hydroxamate resin, most groups typically use the latter [1, 3, 5-6, 8, 16-17]. Several groups have standardized the method using the hydroxamate resin allowing for >99.5% activity recovery [1, 3-4].

Our goal was to optimize the beam energy from the UAB TR-24 cyclotron using aluminium degraders to minimize the production of ^{88}Zr, and determine the optimal conditions for the production of ^{89}Zr. Typically using less target mass allows for more efficient separation, high specific activity and lower contaminants, therefore yttrium sputtered coins were assessed as a target material hypothesizing that the sputtered coins would allow for more control over the target cross sectional area and total mass of yttrium. In this work, we investigated the bombardment of solid yttrium coins and yttrium sputtered target coins as production methods for ^{89}Zr.

2.2 Material and Methods

Aluminum Degrader and Yttrium coins: Aluminum degrader coins were manufactured at the UAB machine shop using 6061 aluminum alloy. The aluminum discs were machined in 0.5 mm, 0.75 mm and 1 mm thickness. Yttrium sheets with a thickness of 1 mm (ESPI metal, Ashland, Oregon) and cut to specified coin size to allow for irradiation in the coin target holder (ACSI, Richmond, Canada). Examples of these coins can be seen in Figure 2-2.

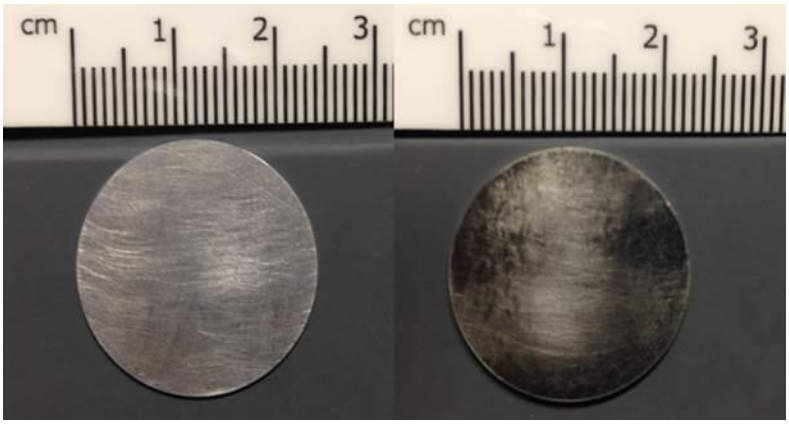

Figure 2-2 6061 Aluminum alloy degrader (left) Yttrium coin (right)

Yttrium (99.9%) sputtered niobium (99.8%) coins, supplied by Advanced Cyclotron Systems, Inc. (ACSI), were investigated as an alternative method of production. The niobium coins had a diameter of 24 mm and a thickness of 1 mm and were cleaned with organic solvent to remove machine oil and lightly sanded. The yttrium was adhered to the coin via magnetron sputtering, vapor deposition, using a mask in the center of the niobium coin with a diameter of 10 mm to contain the sputtering with thickness ranging from 90 μm to 250 μm (Figure 2-3).

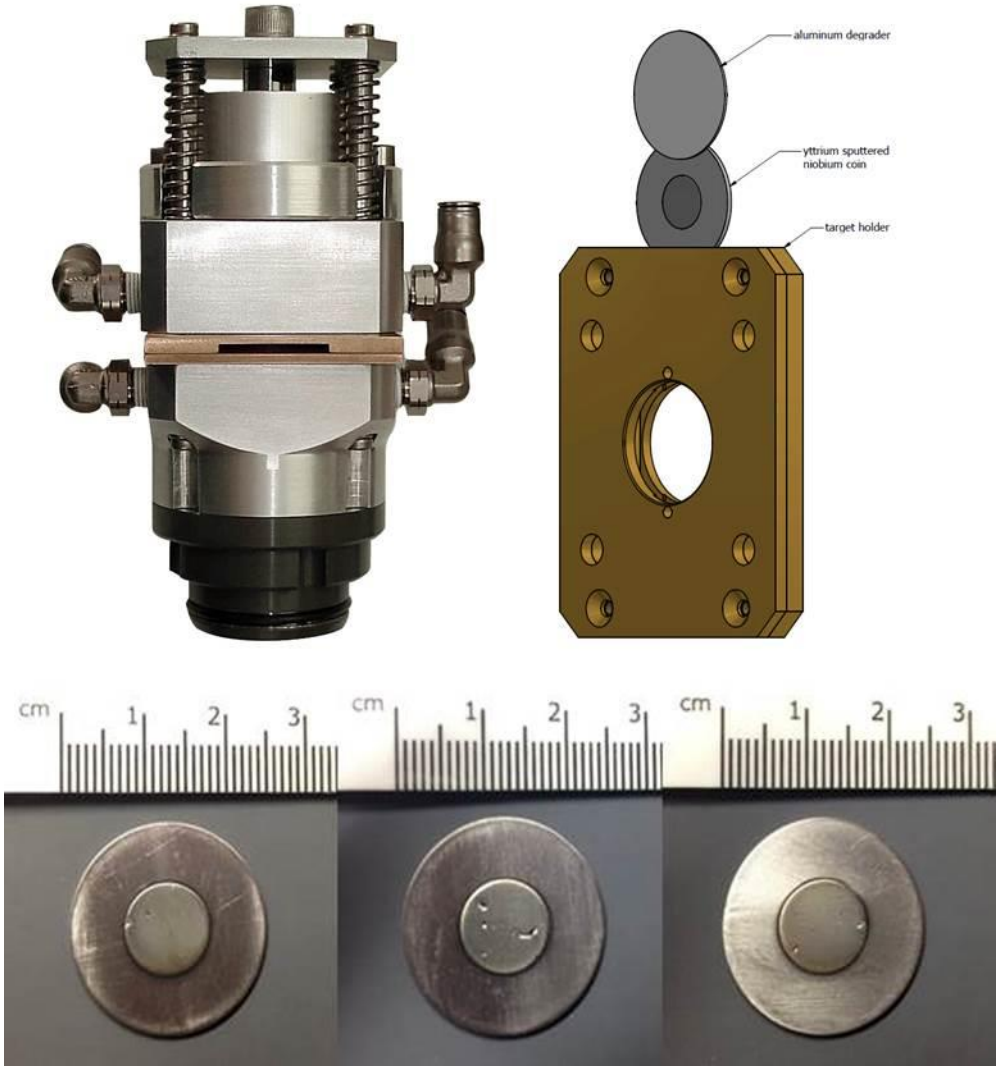

Figure 2-3 Top Left: Cyclotron Coin target holder; Top Right: Disk Assembly; Bottom: Sputtered Coins: Coin 1 (left) 110 µm; Coin 2 (middle) 140 µm; Coin 3 (right) 90 µm

Simulations and Calculations: Transport of Ions in Matter (TRIM) was used to calculate the exit beam energy through the aluminum degrader. This exit energy was used in the theoretical activity yield calculations for the $^{89}Y(p,n)^{89}Zr$ and $^{89}Y(p,2n)^{88}Zr$ (if applicable) using the NNDC website to obtain cross-sections [18] and Stopping and Range of Ions in Matter (SRIM) software [19] to find the correlating range for each energy. This was repeated for several different beam energies and degrader thicknesses.

The theoretical predicted activity was calculated using thin target estimation [20].

$$A = \varphi x \sigma N_{tgt} t \lambda. \qquad (1)$$

where ϕ is the flux of the proton beam, A is the activity of the isotope produced (Bq), x is range in the material (cm), σ is the cross section (cm^2), N_{tgt} is the density of the target nuclei ($atoms/cm^3$), t is the duration of bombardment (s), and λ is the decay constant (s^{-1}).

Optimizing Cyclotron Conditions: Various irradiations of the target using yttrium coins were performed. The beam energy was varied in 100 keV increments until the beam profile provided maximum transmission. The sputtered coins were bombarded for 30 minutes with a 12.5 MeV degraded beam energy using a 0.75 mm aluminum degrader (initial proton energy 17.5 MeV) or two hours with a 12.8 MeV degraded beam energy using a 0.75 mm aluminum degrader (initial proton energy 17.8 MeV) and current was increased for each subsequent coin.

^{89}Zr Radiopurity Analysis: The yttrium coins or yttrium sputtered layers were dissolved in 2 M HCl and an aliquot was removed for gamma spectroscopy analysis using a high purity germanium detector (Ortec, Oak Ridge, Tennessee). The amount of ^{89}Zr and any additional radiocontaminants present in the sample were determined.

Separation and Purification: Conditions for the ^{89}Zr purification are given in Table 2-1 with the average elution volume for recovery of g ^{89}Zr. The irradiated yttrium coins were dissolved in 50 mL of 2 M HCl at 80^{o}C [1]. The entire dissolution process for the coins took about 2 h. Hydroxamate resin was prepared by functionalizing a weak cation exchange resin with hydroxamate groups as previously reported [3]. A column was packed with 850 mg of the hydroxamate resin and loaded with the dissolved yttrium target. Using 2 X 40 mL of 2 M HCl,

the yttrium was eluted from the column followed by 40 mL of water to rinse the HCl off the column. Elution of ^{89}Zr was achieved with a range between of 3 - 14 mL of 1 M oxalic acid.

Complete dissolution of the yttrium layer from the sputtered coin was achieved with 4 mL of 2 M HCl at 80^{o}C in 20 minutes. Yttrium was eluted from a 100 mg of hydroxamate resin column with 2 X 10 mL of 2 M HCl followed with 10 mL of water to wash the column, and ^{89}Zr was eluted with 1 - 1.5 mL of 1 M oxalic acid.

Table 2-1 Separation Parameters

	Yttrium Coins	Sputtered Coins
Original Mass of Yttrium	2 g	20-60 mg
Dissolution Time	2 h	15-30 min
Hydroxamate Resin Mass	850-900 mg	100 mg
Yttrium Elution	80 mL	20 mL
Zr-89 Elution (1 M Oxalic Acid)	7.3 mL	1.2 mL

Specific Activity Analysis and Radiolabeling: DFO-SCN was dissolved in DMSO to make a stock solution and serial dilutions were prepared using 1 M HEPES buffer as the diluent. 20 μCi of the prepared ^{89}Zr were added to each dilution and DTPA was used to challenge the solution. The resulting solutions were analyzed using TLC to determine the effective specific activity [1, 3, 21]. Solutions were also obtained from several samples prior to and after the purification process. These solutions were analyzed by ICP-MS (Agilent, Santa Clara, California) and the amount of yttrium, zirconium, aluminum, niobium, and iron in each sample was measured. To examine the utility of the purified ^{89}Zr, a typical antibody labeling was conducted [2, 21-23]. DFO-Trastuzumab and ^{89}Zr were combined to give a specific activity of 8 μCi/μg. The solution

was incubated at 37°C with agitation for one hour. The solution was challenged with 50 mM DTPA for 5 minutes. Results were then analyzed using ITLC plates with 50 mM DTPA as the mobile phase on TLC scanner (Eckert & Ziegler, Berlin, Germany).

2.3 Results

Simulations and Calculations: The simulation for 17.8 MeV beam energy propagating through a 0.75 mm aluminum degrader, and the projected path of a 17.8 MeV beam through a 0.75 mm aluminum degrader and 1 mm yttrium coin can be seen in Figure 2-4. These simulations show the range of the beam in the material and the deviation of the beam from the center. This illustrates that the beam will not propagate through the entirety of the material and no contamination of the water cooling system will occur.

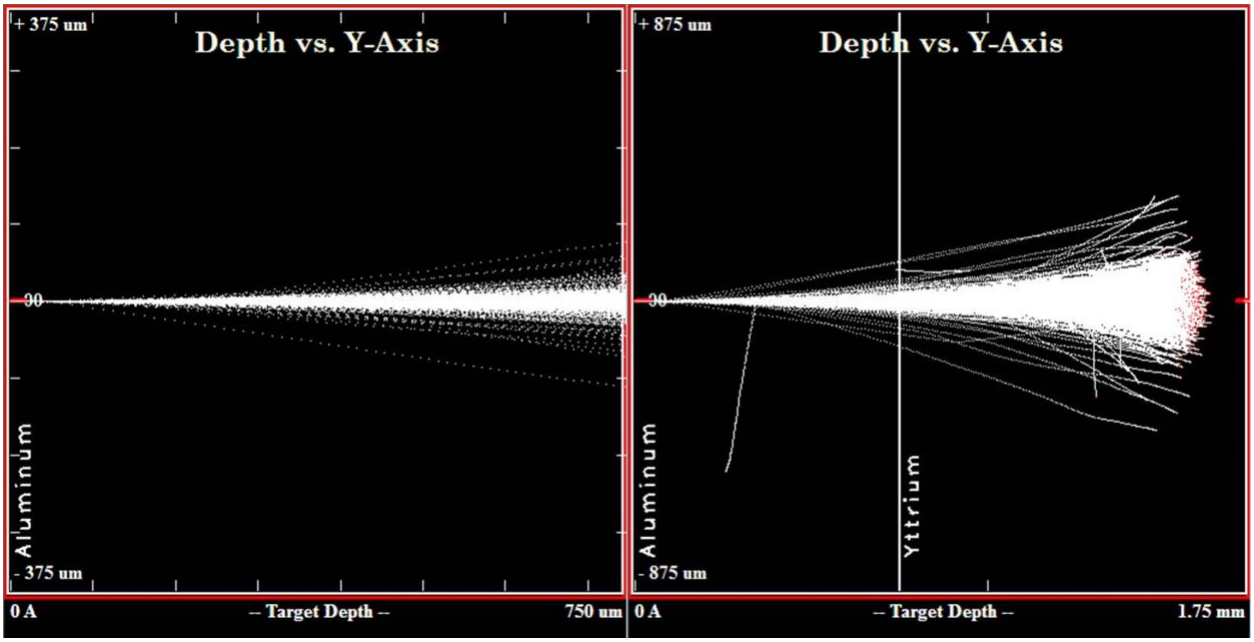

Figure 2-4 Projected path of the proton beam through matter. 0.75 mm Aluminum (left), 0.75 mm Aluminum and 1 mm Yttrium (right) [19]

A simulation for the sputtered coins with a 17.8 MeV proton beam energy and a 0.75 mm aluminum degrader was also conducted. The energy exiting the aluminum degrader was calculated to be 12.8 MeV and the exiting energy for the yttrium layer was 10.9 MeV. Although this energy may activate the niobium backing of the sputtered coins, there are several advantages to using niobium. Niobium is chemically inert, affordable and provides a reliable sputtering support material for yttrium.

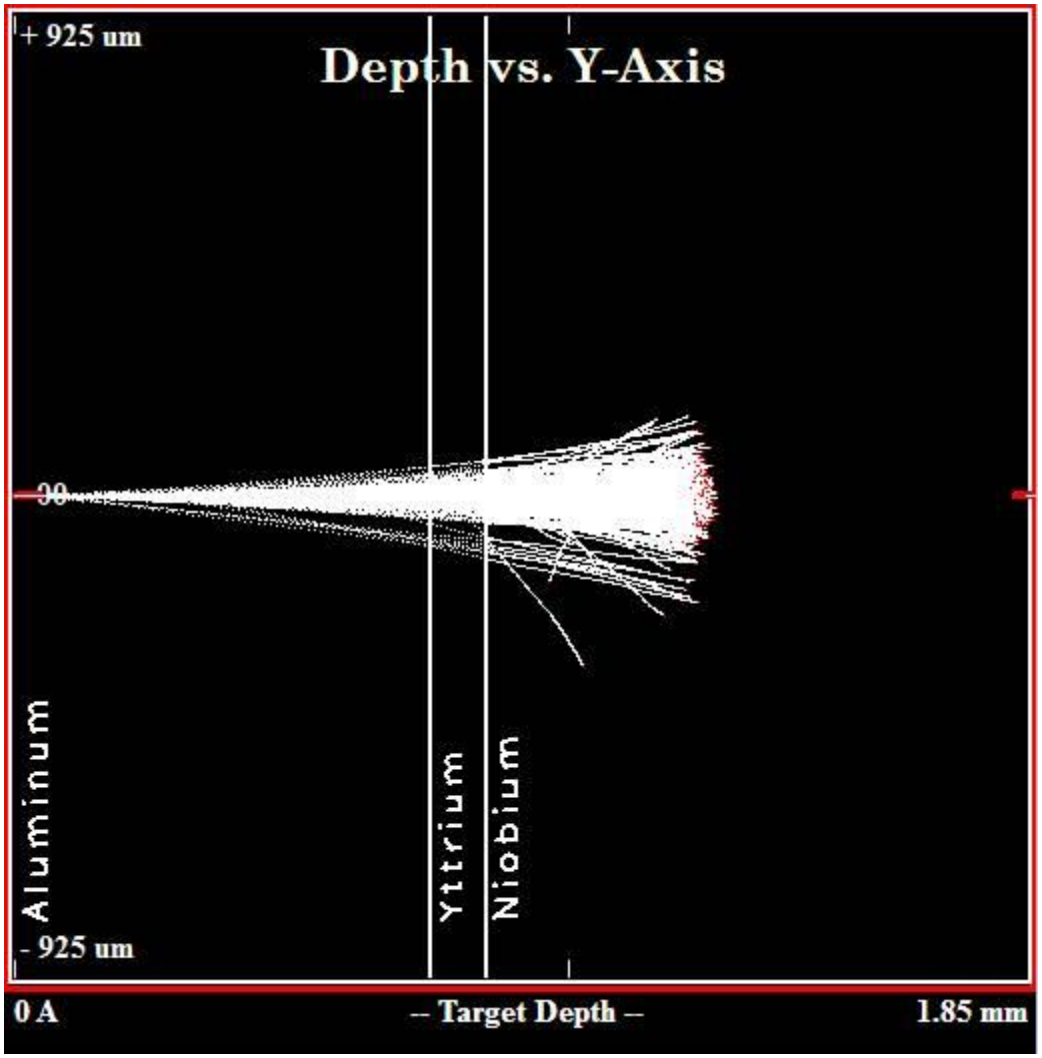

Figure 2-5 TRIM simulation for the sputtered Coin [19]

Figure 2-5 shows that the beam propagates through all three materials and stops in the niobium backing. The following table (Table 2-2) shows the results obtained from performing the Monte Carlo simulations for the energy degradation through the aluminum coin and the theoretical activity of ^{89}Zr and ^{88}Zr (if applicable). The calculated energy threshold for ^{88}Zr production is 13.08 MeV, which can be considered the upper limit on the beam energy for the production of ^{89}Zr.

Table 2-2 ^{89}Zr Production using a current of 10 μA and irradiation time of 20 minutes

Beam Energy (MeV)	Aluminum Thickness (mm)	Transmitted Energy (MeV)	Predicted Activity Zr-89 (mCi)	Predicted Activity Zr-88 (μCi)
16	0.5	12.5	3.75	NA
16.5	0.5	13.1	4.41	NA
16.5	0.75	11.1	2.51	NA
16.5	1	8.86	0.57	NA
16.7	0.5	12.5	3.75	NA
17	0.5	13.7	5.03	0.05
17	0.75	11.8	3.11	NA
17	1	9.65	0.98	NA
17.5	0.5	14.3	6.18	1.11
17.5	0.75	12.5	3.75	NA
17.5	1	10.4	1.46	NA
17.8	0.75	12.8	3.93	NA
18	0.5	14.9	6.73	3.99
Calculated Threshold Energy for Zr-88 using Q-value and Coulomb Barrier			13.08 MeV	

Optimizing Cyclotron Conditions: The lowest beam energy for an optimal profile and transmission was determined through iterations of the ion source and magnet system settings on the cyclotron. The lowest effective beam energy of 17 MeV gave a transmission of 81%. The best theoretical energy for the production of ^{89}Zr using the aluminum degrader would be at 17.8 MeV using a 0.75 mm thick aluminum degrader.

The theoretical calculations and activity of each coin after bombardment are given in Table 2-3. Although there are four yttrium coins listed in Table 2-3, six irradiation attempts were made for each type of coin. Two of the yttrium coins were damaged during a 2 h irradiation using 17.8 MeV beam energy as can be seen in Figure 2-6.

Figure 2-6 Damage to the yttrium coins (Y 5, Y 6) with 2 h irradiation with 12.8 MeV transmitted beam energy (17.8 MeV initial beam energy) and 40 μA current.

The following figure (Figure 2-7) shows the sputtered coins after various irradiation conditions. The physical appearance of the coins clearly shows an increase in scorching as the current and duration of irradiation increases.

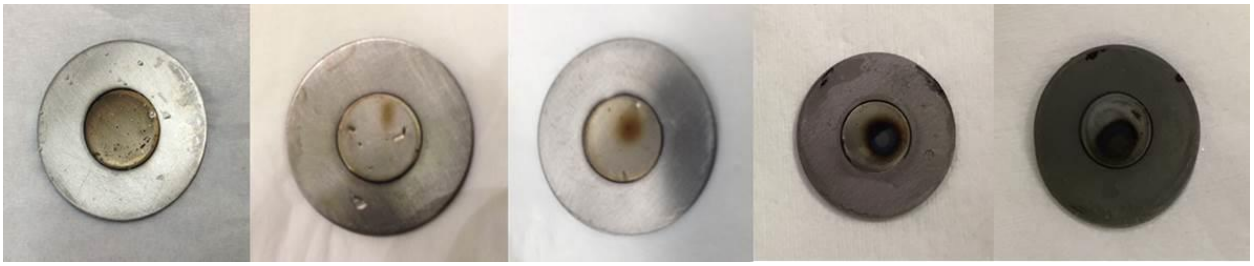

Figure 2-7 (from left to right) Sputtered Coin 1 t=30 min, 10 μA, 12.5 MeV; Sputtered Coin 2 t=30 min, 21 μA, 12.5 MeV; Sputtered Coin 3 t=30 min, 30 μA, 12.5 MeV; Sputtered Coin 6 t=2 h, 40 μA, 12.8 MeV; Sputtered Coin 5 t=2 h, 45 μA, 12.8 MeV

Radiopurity Analysis: The following table (Table 2-3) provides a summary of the radionuclides found in the analysis of the coin targets.

Table 2-3 Activity measured on HPGe for irradiated targets

Coin	Yttrium Thickness	Isotope	$A_{Measured}$ of Coin	$A_{Theoretical}$	Transmitted Energy	Current	Time
Y 1	1 mm	^{89}Zr	5.13 mCi	4.71 mCi	14.9 MeV	7 μA	20 min
		^{88}Zr	13.6 μCi	3.99 μCi			
Y 2	1 mm	^{89}Zr	3.15 mCi	3.18 mCi	12.5 MeV	8.5 μA	20 min
		^{88}Zr	Not Observed	NA			
Y 3	1 mm	^{89}Zr	8.08 mCi	10.06 mCi	13.7 MeV	20 μA	20 min
		^{88}Zr	8.57 μCi	0.05 μCi			
Y 4	1 mm	^{89}Zr	66.24 mCi	89.26 mCi	12.8 MeV	40 μA	2 h
		^{88}Zr	Not Observed	NA			
Sputtered Coin 1	110 μm	^{89}Zr	1.63 mCi	1.82 mCi	12.5 MeV	10 μA	30 min
		^{88}Zr	Not Observed	----			
Sputtered Coin 2	140 μm	^{89}Zr	3.94 mCi	4.86 mCi	12.5 MeV	21 μA	30 min
		^{88}Zr	Not Observed	----			
Sputtered Coin 3	90 μm	^{89}Zr	2.60 mCi	4.46 mCi	12.5 MeV	30 μA	30 min
		^{88}Zr	Not Observed	----			
Sputtered Coin 4	220 μm	^{89}Zr	25.37 mCi	31.28 mCi	12.5 MeV	40 μA	2 h
		^{88}Zr	Not Observed	----			
Sputtered Coin 5	210 μm	^{89}Zr	43.8 mCi	45.27 mCi	12.8 MeV	45 μA	2 h
		^{88}Zr	Not Observed	----			
Sputtered Coin 6	90 μm	^{89}Zr	21.9 mCi	23.09 mCi	12.8 MeV	40 μA	2 h
		^{88}Zr	Not Observed	----			

The first yttrium coin was irradiated with an initial beam energy of 18 MeV degraded to 14.9 MeV. As these conditions resulted in significant amounts of ^{88}Zr, the target was not dissolved for analysis. The coin, however, was analyzed for ^{88}Zr once the ^{89}Zr had decayed.

Table 2-3 shows that ^{88}Zr is still present with the beam energy only degraded to 13.7 MeV. In order to obtain minimal ^{88}Zr with maximum ^{89}Zr, an incident beam energy of 17.5 MeV or 17.8 MeV was used in subsequent irradiations with a 0.75 mm aluminum degrader to give a transmitted beam energy of 12.5 MeV or 12.8 MeV, respectively. This is verified in the sputtered coin targets.

Separation and Purification: Following purification of the irradiated yttrium coins, 88.3 ± 4.9% of the loaded ^{89}Zr was recovered in an average of 7.3 mL of 1 M oxalic acid. Following purification of the sputtered coins 97.9 ± 2.8% of the loaded ^{89}Zr was obtained in an average of 1.2 mL of 1 M oxalic acid as shown in Table 2-4. In Table 2-4, A_{Loaded} represents the activity that was recovered after dissolution and loaded onto the column, Volume represents the recovery volume for the bulk activity elution (A_{Eluted}), and the Total Yield, % represents the total activity recovered overall.

Table 2-4 Purification yield of ^{89}Zr

Coin	A_{Loaded} on Column (mCi)	Bulk Collection Volume (mL)	Total Volume (mL)	Bulk A_{Eluted} (mCi)	Elution Yield, %	Total Yield, %
Y 1	Not Purified					
Y 2	8.3	12	14	5.5	66.3	92.1
Y 3	3.3	2	3	2.6	78.8	82.8
Y 4	53.4	3	5	47.8	88.6	89.9
Sputtered Coin 1 (1)	Not Purified					
Sputtered Coin 2 (2)	2	1	1.25	1.9	95	99.5
Sputtered Coin 3 (3)	2	1	1.25	1.8	90	96
Sputtered Coin 4 (9A)	25.3	0.5	1	21.3	84.2	93.8
Sputtered Coin 5 (4A)	33.9	1	1.5	33.8	99.7	100
Sputtered Coin 6 (1A)	12.8	0.5	1	11.1	86.7	100

^{89}Zr Analysis: The ^{89}Zr effective specific activity was determined using DFO titration with values of 20.3 mCi/μmol for the solid yttrium coin productions and 108 ± 7 mCi/μmol for the yttrium sputtered coin productions. The ICP-MS analysis of the yttrium coin and the sputtered coins showed 99.99% yttrium removed with 178 μg of yttrium in the final solution and 99.93 - 100% of yttrium was removed with 0 - 42 μg of yttrium in the final solution, respectively. ICP-

MS analysis was used to determine the concentration of other impurities present in the solution, such as zirconium, aluminum and iron. Niobium for all samples were below the detection limits of the instrument. Table 2-5 provides the concentrations found each element in the solutions. The specific activity calculated for the Y 4 coin and the sputtered coins 2, 3 and 4 using the concentration of Zr found via ICP-MS was 140 ± 2 mCi/μmol, 300 ± 30 mCi/μmol, 410 ± 60 mCi/μmol and 1719 ± 5 mCi/μmol, respectively. DFO-Trastuzumab was successfully labeled with ^{89}Zr produced from the sputtered yttrium coins with yields between 98% - 100%.

Table 2-5 ICP-MS analysis of yttrium coin and the sputtered coin

Sample		Y-89 (ppb)	Zr-90 (ppb)	Al-27 (ppb)	Fe-56 (ppb)
Yttrium Coin	Crude	$3.381(\pm0.017)\times10^{7}$	$3.8(\pm0.4)\times10^{4}$	$10(\pm0.2)\times10^{6}$	$7.6(\pm0.3)\times10^{5}$
	Purified	$3.02(\pm0.08)\times10^{3}$	$1.039(\pm0.015)\times10^{4}$	$5(\pm3)\times10^{2}$	$5.4(\pm0.2)\times10^{2}$
Sputtered Coin 2	Crude	$7.58(\pm0.03)\times10^{6}$	$6.5(\pm0.5)\times10^{3}$	$9(\pm4)\times10^{4}$	$7.35(\pm0.16)\times10^{4}$
	Purified	$5.47(\pm0.09)\times10^{3}$	$5.9(\pm0.6)\times10^{2}$	$6.2(\pm0.3)\times10^{3}$	$7.1(\pm0.4)\times10^{3}$
Sputtered Coin 3	Crude	$4.49(\pm0.05)\times10^{6}$	$4.5(\pm0.4)\times10^{3}$	$4(\pm3)\times10^{4}$	$7.2(\pm0.9)\times10^{4}$
	Purified	$6.3(\pm0.5)\times10^{2}$	$4.0(\pm0.6)\times10^{2}$	$2.1(\pm0.9)\times10^{4}$	$3.29(\pm0.09)\times10^{4}$
Sputtered Coin 4	Crude	$1.639(\pm0.014)\times10^{7}$	$2.23(\pm0.08)\times10^{3}$	$9.9(\pm1.9)\times10^{3}$	$8.07(\pm0.16)\times10^{3}$
	Purified	$5.36(\pm0.19)\times10^{2}$	$2.261(\pm0.006)\times10^{3}$	$9(\pm3)\times10^{2}$	$9.0(\pm0.3)\times10^{2}$

2.4 Discussion

Sputtered yttrium coins are an alternative and feasible route for the production of ^{89}Zr with high ^{89}Zr recovery and easy processing. The difference in the activity measured on sputtered coins to the theoretical yields may be due to error in the thickness used in the theoretical calculations.

The thickness of the sputtered coins was determined using the mass of the yttrium sputtered onto the niobium coin and likely, the yttrium is not at 100% theoretical density. We found that the sputtered coins with a 0.75 mm aluminum degrader bombarded with a beam energy of 17.8 MeV giving a transmitted energy of 12.8 MeV on the sputtered coins and a current of 40 μA for 2 hours produced the best results. No ^{88}Zr was observed in the analysis of the sputtered coins due to the degradation of the beam, providing 100% radionuclidic purity similar to the reports from low energy beam production of ^{89}Zr in literature [24]. The majority of activity for the sputtered coins were recovered in 1 mL (2 aliquots) of 1 M oxalic acid which was comparable to Holland et al. who reported >99% recovery in 3 mL [3]. We were able to obtain a specific activity of 108 ± 7 mCi/μmol which is somewhat lower than Holland et al. (470-1195 mCi/μmol) [3], however this may be due to the lower amounts of activity produced during our scale up phase. ICP-MS analysis of the yttrium coin and the sputtered coins showed 99.99% yttrium removed with 178 μg of yttrium in the final solution and 99.93-100% of yttrium was removed with 0-42 μg of yttrium in the final solution, respectively. Furthermore, the ICP-MS analysis showed a higher concentration of zirconium in the production from the solid yttrium coins contributing to the lower specific activity obtained when using this method. The sputtered coins showed higher concentrations of aluminum and iron than the yttrium coin. Further investigations for these trends are ongoing. DFO-trastuzumab was successful labeled with the purified activity from the sputtered coins giving yields of 98-100% with a concentration of 13.1 mCi/mL of buffered and pH adjusted ^{89}Zr. This is consistent with other reported labeling yields. Marquez et al. reported >95% yield with pertuzumab and Holland et al. reported >70% yielding with DFO-trastuzumab [2, 21].

In the future, longer irradiations of sputtered coins with higher currents will be performed using a 0.75 mm aluminum degrader and 17.8 MeV incident beam energy and a transmission energy of 12.8 MeV. Separation methods to optimize specific activity will be investigated as well as automated processes for the purification and recovery of ^{89}Zr.

2.5 Conclusions

The use of sputtered yttrium on niobium coins have shown to be an effective and alternative means of production of ^{89}Zr. The degradation of the proton beam via aluminum degrader to <13 MeV eliminated the production of ^{88}Zr and allowed for 100% radionuclidic purity. The integrity of the sputtered coins was not compromised, unlike that of the yttrium coins at higher current and longer irradiation periods. The sputtered coins resulted in more control over yttrium mass and the target cross sectional area. This allowed for an efficient separation of ^{89}Zr from the target material and a dissolution time that is significantly shorter than the yttrium coins that resulted in a product with higher specific activity.

2.6 Acknowledgments

Special thanks to Harvey Doane, Jason Rider and Brian Books from the UAB Cyclotron Facility and Daniel Long and Chris Shoemaker from the UAB Machine Shop.

2.7 References

1. Wooten, A. L. M., E.; Schweitzer, G. D.; Lawrence, L. A.; Mebrahtu, E.; Lewis, B. C.; Lapi, S. E., Routine Production of ^{89}Zr Using Automated Module. *Appl. Sci.* **2013,** *3*, 593-613.
2. Marquez, B. V.; Ikotun, O. F.; Zheleznyak, A.; Wright, B.; Hari-Raj, A.; Pierce, R. A.; Lapi, S. E., Evaluation of (89)Zr-pertuzumab in Breast cancer xenografts. *Mol Pharm* **2014,** *11* (11), 3988-95.

3. Holland, J. P.; Sheh, Y.; Lewis, J. S., Standardized methods for the production of high specific-activity zirconium-89. *Nucl Med Biol* **2009,** *36* (7), 729-39.
4. Van Dongen, G. A. M. S.; Visser, G. W. M.; Lub-de Hooge, M. N.; de Vries, E. G.; Perk, L. R., Immuno-PET: A navigator in monoclonal antibody development and applications. *Oncologist* **2007,** *12*, 1379-1389.
5. Deri, M. A.; Zeglis, B. M.; Francesconi, L. C.; Lewis, J. S., PET imaging with (8)(9)Zr: from radiochemistry to the clinic. *Nucl Med Biol* **2013,** *40* (1), 3-14.
6. Kandil, S. A.; Scholten, B.; Saleh, Z. A.; Youssef, A. M.; Qaim, S. M.; Coenen, H. H., A comparative study on the separation of radiozirconium via ion-exchange and solvent extraction techniques, with particular reference to the production of ^{88}Zr and ^{89}Zr in proton induced reactions on yttrium. *J. Radioanal. Nucl. Chem.* **2007,** *274*, 45-52.
7. Brasse, D.; Nonat, A., Radiometals: towards a new success story in nuclear imaging? *Dalton Trans* **2015,** *44* (11), 4845-58.
8. Kasbollah, A.; Eu, P.; Cowell, S.; Deb, P., Review on production of 89Zr in a medical cyclotron for PET radiopharmaceuticals. *J Nucl Med Technol* **2013,** *41* (1), 35-41.
9. Sadeghi, M. E., M.; Bakhtiari, M., Accelerator production of the positron emitter zirconium-89. *Annals of Nuclear Energy* **2012,** *41*, 97-103.
10. Meijs, W. E.; Herscheid, J. D.; Haisma, H. J.; Wijbrandts, R.; Van Langevelde, F.; Van Leuffen, P. J.; Mooy, R.; Pinedo, H. M., Production of Highly Pure No-carrier Added ^{89}Zr for the Labelling of Antibodies with a Positron Emitter. *Appl. Radiat. Isot.* **1994,** *45*, 1143-1147.
11. Pandey, M. K.; Bansal, A.; Engelbrecht, H. P.; Byrne, J. F.; Packard, A. B.; DeGrado, T. R., Improved production and processing of (8)(9)Zr using a solution target. *Nucl Med Biol* **2016,** *43* (1), 97-100.
12. Gritsyna, V. T.; Klyucharev, A. P.; Remaev, V. V.; Resgetova, L. N., Ratio of the cross sections for the production of the isomer and ground states of nuclei in the (p,n) reaction at the energies from the threshold to 20 MeV. *Sov. Phys. JETS* **1963,** *17*, 1186-1189.
13. Saha, G. B.; Porile, N. T.; Yaffe, L., (p, xn) and (p,pxn) Reactions of Yttrium-89 with 5—85-MeV Protons. *Phys. Rev.* **1966,** *144*, 962-971.
14. Wenrong, Z. Q., S.; Hanlin, L.; Weixiang, Y., Investigation ^{89}Y(p,n)^{89}Zr,^{89}Y(p,2n)^{88}Zr and ^{89}Y(p,pn)^{88}Y reactions up to 22 MeV. *Chinese Journal of Nuclear Physics* **1992,** *24* (11), 7-14.
15. Mustafa, M. G.; West, H. I., Jr.; O'Brien, H.; Lanier, R. G.; Benhamou, M.; Tamura, T., Measurements and a direct-reaction-plus-Hauser-Feshbach analysis of 89Y(p,n)89Zr, 89Y(p,2n)88, and 89Y(p,pn)88Y reactions up to 40 MeV. *Phys Rev C Nucl Phys* **1988,** *38* (4), 1624-1637.
16. deJesus, O. T.; Nickles, R. J., Production and Purification of ^{89}Zr, a Potential PET Antibody Label. *Appl Radiat Isot* **1990,** *41*, 789-790.
17. Severin, G. W.; Engle, J. W.; Barnhart, T. E.; Nickles, R. J., 89Zr radiochemistry for positron emission tomography. *Med Chem* **2011,** *7* (5), 389-94.
18. National Nuclear Data Center (nndc). http://www.nndc.bnl.gov/exfor/exfor.htm (accessed 18 March).
19. Ziegler, J. F. *SRIM*, 2013; Web, 2013.
20. Ehmann, W. D.; Vance, D. E., Radiochemistry and Nuclear Methods of Analysis. Johnn Wiley & Sons, Inc: New York, NY, 1991; pp 92-93, 141-142.

21. Holland, J. P.; Caldas-Lopes, E.; Divilov, V.; Longo, V. A.; Taldone, T.; Zatorska, D.; Chiosis, G.; Lewis, J. S., Measuring the pharmacodynamic effects of a novel Hsp90 inhibitor on HER2/neu expression in mice using Zr-DFO-trastuzumab. *PLoS One* **2010,** *5* (1), e8859.
22. Ikotun, O. F.; Marquez, B. V.; Huang, C.; Masuko, K.; Daiji, M.; Masuko, T.; McConathy, J.; Lapi, S. E., Imaging the L-type amino acid transporter-1 (LAT1) with Zr-89 immunoPET. *PLoS One* **2013,** *8* (10), e77476.
23. Chang, A. J.; De Silva, R. A.; Lapi, S. E., Development and characterization of 89Zr-labeled panitumumab for immuno-positron emission tomographic imaging of the epidermal growth factor receptor. *Mol Imaging* **2013,** *12* (1), 17-27.
24. Dabkowski, A. M. P., S. J.; Talboys, M.; Marshall, C. In *Optimization of Cyclotron Production for Radiometal of Zirconium 89,* Proceedings of the II Symposium on Positron Emission Tomography,, 2014; pp 1479-1482.

Chapter 3

Radiochemical separation of ^{89}Zr from yttrium utilizing an inorganic ion-exchanger

[This work has been presented previously at the 255th ACS National Meeting as "Inorganic ion-exchangers for radiochemical separations of Y/Zr and Ti/Sc," Stacy L Queern, Cienna L. Manderbach, Cathy S. Cutler, Dmitri G. Medvedev, Suzanne E. Lapi, and Jonathan M. Fitzsimmons, **March 2018**]

3.1 Introduction

Zirconium-89 (^{89}Zr) is a positron emitter with a half-life of 78.4 hours and uses in medical imaging applications. [1-3]. The long half-life of ^{89}Zr can allow for imaging at longer time points and matches well with the biological half-life of intact antibodies making it of high interest for PET imaging [3-5]. The production of ^{89}Zr is typically via irradiation of an yttrium (Y) target which requires the removal of the Y before the ^{89}Zr can be used in radiolabeling. Current separation of ^{89}Zr from Y involves adsorption of ^{89}Zr on hydroxamate or Zr resin (Triskem) after dissolution of the target material in 2 M hydrochloric acid (HCl). The Y is eluted off the column using 2 M HCl and then the column is washed with high purity water [1, 6-7]. The ^{89}Zr is eluted using heated 1 M oxalic acid [1, 6-7]. Although this is a relatively simple procedure for the purification of ^{89}Zr, there are a few minor issues that can be improved upon. The heating of oxalic acid can make it more difficult to implement this method into an automated system and the oxalic acid is somewhat undesirable eluent as it needs to be removed before injection due to toxicity issues [1, 8].

Crystalline silicotitanate (CST) is an inorganic exchange resin that has been used in the purification of aqueous radioactive waste. In particular, the characteristics of poorly crystalline silicotitanate (pCST) and highly crystalline silicotitanate (C-CST) have been reviewed mainly for the waste removal of ^{137}Cs. pCST offers some advantageous adsorption properties over the C-CST. Since pCST is heated less during formation, the particle size produced is smaller with rough faces and edges [9-10]. These characteristics allow for an increased surface to volume ratio to allow for more interactions but with less stable adsorption, thus increasing recovery of the target isotope relative to C-CST [9-11]. pCST has shown to have strong stability to radiation

and selectivity for cesium (Cs) and strontium (Sr) metals making it the preferred resin to separate Cs and Sr from nuclear waste [9-10, 12]. In unpublished work conducted at Brookhaven National Laboratory due to general interest in inorganic resins for radiation stability, pCST was found to have a high affinity for Zr while having a low affinity for Y and thus is a promising support material in the separation of Zr from Y.

Iminodiacetic acid (IDA) is a chelator that is currently being used in patients for hepatobiliary (HIDA) scans [13]. IDA is a tridentate ligand (Figure 3-1), making it a weak chelator for ^{89}Zr which is tetravalent.

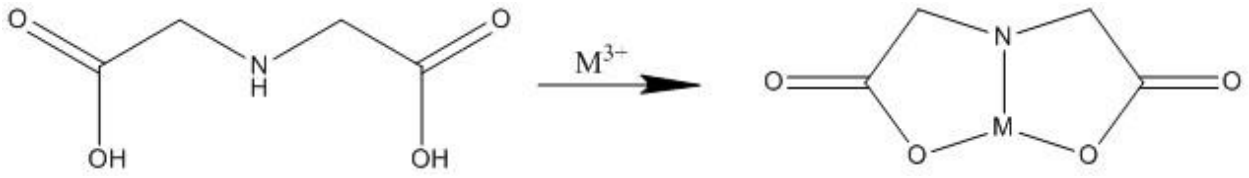

Figure 3-1 IDA chelation as a tridentate ligand

These characteristics allow for the potential use of IDA to remove ^{89}Zr from the pCST column while maintaining a relatively unstable complex as not to interfere with subsequent labeling chemistry. The aim of our work is to evaluate suitability of pCST for the separation of ^{89}Zr using IDA as an eluant to allow for ease in automating the separation system and potentially eliminating the need to remove the IDA chelator before injection.

3.2 Materials and Methods

Measurement of Distribution Coefficient: K_d studies for Zr and Y were carried out using pCST resin. Stock solutions of 0.5 M ammonium acetate (NH_4OAc) at pH 3 and 0.1 M iminodiacetic acid (IDA) at pH 3 with 30 ppm Zr and 30 ppm Y were prepared. 30 mg of resin was weighed

out into 15 mL falcon tubes. 5 mL of IDA was introduced to the resin with 100 μL of metal solution. The samples were placed on a shaker and allowed to reach equilibrium for at least 24 hours. 1.5 mL aliquots of the samples were taken and centrifuged to separate the resin from the solution. 10 μL of the supernatant was removed for ICP-MS analysis and diluted with 5 mL of 2% nitric acid. The K_d was calculated with the following equation where K_d is binding affinity, C_i is initial metal concentration, C_a is final metal concentration, V_x is total volume (mL), and M_x is mass of resin (g).

$$K_d = \frac{C_i - C_a}{C_a} \times \frac{V_x}{M_x} \quad (1)$$

Data analysis was completed using *Prism* version 7 and p-values calculated using one-way ANOVA multiple comparison with 95% confidence where $p < 0.05$ was considered significant.

^{89}Zr Purification with pCST : A 0.1 mL bed volume PEEK column was loaded with pCST resin and conditioned with 10 mL of 0.5 M ammonium acetate at pH 3 at a flow rate of 0.1 mL/min. 2 mCi of crude ^{89}Zr solution containing ~11 mg of Y in 2 M HCl obtained from the UAB Cyclotron Facility was diluted to 2.5 mL using 0.5 M ammonium acetate at pH 3 and loaded onto the column at a flow rate of 0.1 mL/min. The flow through of this loading was collected in 500 μL fractions. The Y was then washed off the column using 0.5 M ammonium acetate at pH 3 at a flow rate of 0.1 mL/min in ten 500 μL fractions (total volume of 5 mL). ^{89}Zr was eluted off the column using 0.1 M IDA at pH 3 with a flow rate of 0.1 mL/min in twenty 500 μL fractions (total volume of 10 mL). 10 μL aliquots of each fraction were removed and diluted with 2% nitric acid for ICP-MS analysis of Y and Ti.

^{89}Zr Labeling and Specific Activity: The antibody panitumumab, was purchased from Vectibix (Thousand Oaks, CA), the chelator deferoxamine (DFO-SCN) was purchased from Macrocyclics (Plano, TX) and all other reagents were purchased through Fisher Scientific. For test labeling studies with ^{89}Zr, panitumumab was conjugated with DFO-SCN using a 10:1 molar ratio of antibody to chelator where 15 μL of 20 mg/mL DFO-SCN, 150 μL of 8 mg/mL panitumumab and 135 μL of 0.1 sodium carbonate buffer pH 9 were allowed to react for 1 h on a thermoshaker set for 37°C at 350 rpm [14]. The final product was purified on a Zeba spin desalting column (40 kDa molecular weight cutoff). The labeling was carried out using 12.5 μL of 1 mg/mL DFO-panitumumab which was aliquoted into a microcentrifuge for each labeling. ^{89}Zr-IDA was neutralized using 1 M HEPES. A ~6 μL aliquot (5-7 μCi) was added to each of the corresponding labeling microcentrifuge tubes. For comparison to the standard method, ^{89}Zr-oxalate, produced in house, was neutralized using 1 M HEPES and 2 M NaOH [6]. 50 μCi (~6 μL) of the neutralized standard ^{89}Zr was added to each of the corresponding labeling microcentrifuge tubes. Then the microcentrifuge tubes were brought to 30 μL in final volume using 1 M HEPES (~11.5 μL). The microcentrifuge tubes were placed on a thermoshaker set for 37°C at 300 rpm for one hour and then challenged with 50 mM DTPA for 5 minutes. A 1 μL aliquot of each labeling (both prior to the DTPA challenge and after) was spotted on iTLC-SG, glass microfiber chromatography paper impregnated with silica gel (Agilent, CA) and developed with 50 mM DTPA as mobile phase and analyzed on AR-2000 Radio-TLC imaging scanner (Eckert & Ziegler, MA) to determine the labeling efficiency.

Effective specific activity (ESA) was determined using the DFO- titration method [1, 6]. A stock solution of 5 mg/mL DFO in DMSO was serially diluted with 1 M HEPES. Each 200 μL dilution

had ~25 μCi (~30 μL) of ^{89}Zr-IDA added to each tube. The tubes were placed on a thermoshaker set for 37°C at 300 rpm for one hour and then challenged with 50 mM DTPA. A 1 μL aliquot of each dilution was spotted on the iTLC-SG paper, developed with 50 mM DTPA as the mobile phase, then analyzed on an AR-2000 Radio-TLC imaging scanner.

3.3 Results and Discussion

Distribution Coefficient Study: Ideally, for the distribution coefficient, K_d, values, the difference between the metals in the solvent should be large where the larger of the two values indicates the ion has a stronger affinity for the resin under the conditions studied. This means the metal with the lower K_d value will elute off in that solvent while the metal with the larger K_d value will be retained on the resin. These ideal conditions can be seen in Figure 3-2 for 0.5 M ammonium acetate pH 3 where the K_d value for Zr was 7700±500 mL/g and the K_d value for Y was 590±90 mL/g. The K_d values for the 0.1 M IDA pH 3 for Zr and Y were 730±80 mL/g and 840±110 mL/g, respectively. The large difference in the distribution coefficients between the Zr and Y for the 0.5 M NH_4OAc pH 3 shows that the Zr has a stronger affinity for the pCST resin and will be retained on the resin while the Y is washed off. Although there is little difference between the K_d values for 0.1 M IDA pH 3, this shows that Zr has a low affinity for the resin under the conditions studied. This data indicates the elution order should be 0.5 M ammonium acetate pH 3 to remove the Y and then 0.1 M IDA pH 3 to collect the Zr from the resin.

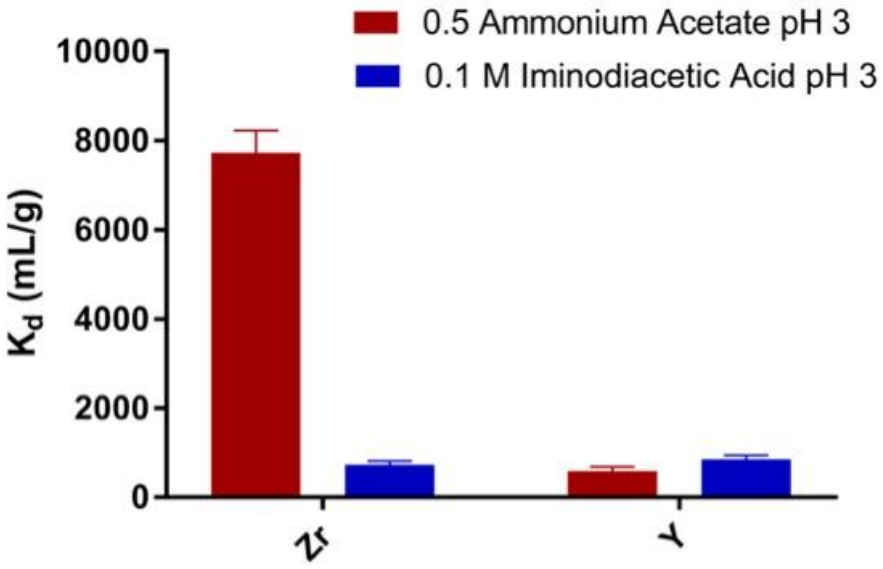

Figure 3-2 Distribution coefficient study with 0.1 M NH_4OAc (pH 3) and 0.1 M IDA (pH 3)

^{89}Zr Separation with pCST: The activity elution profile shown in Figure 3-3 shows less than 6±3% ^{89}Zr breakthrough in the first 15 fractions (7.5 mL) and 80±11% of ^{89}Zr was recovered overall (10 mL) with 58±16% in fraction 17 and 18 (1 mL). These small-scale separations showed repeatable results with the majority of the activity being collected the second IDA elution fraction.

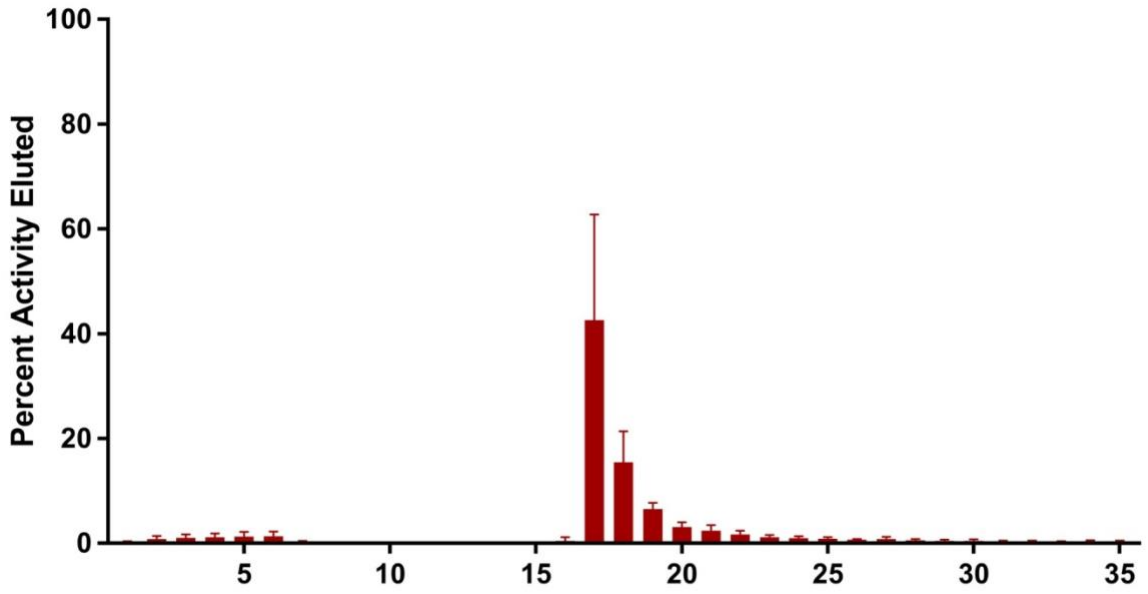

Figure 3-3 Activity elution profile illustrating average radioactivity per fraction

ICP-MS was used to investigate the amount of Y and Ti found in each fraction (Y being the target material and Ti as part of the pCST crystalline structure). The Y and Ti elution profile are provided in Figure 3-4. This figure shows that while both Y and Ti are present in the early fractions, they are no longer eluted after fraction 8. The Ti analysis shows that any loose metal or resin has been removed before the collection of the ^{89}Zr in fractions 17 and 18.

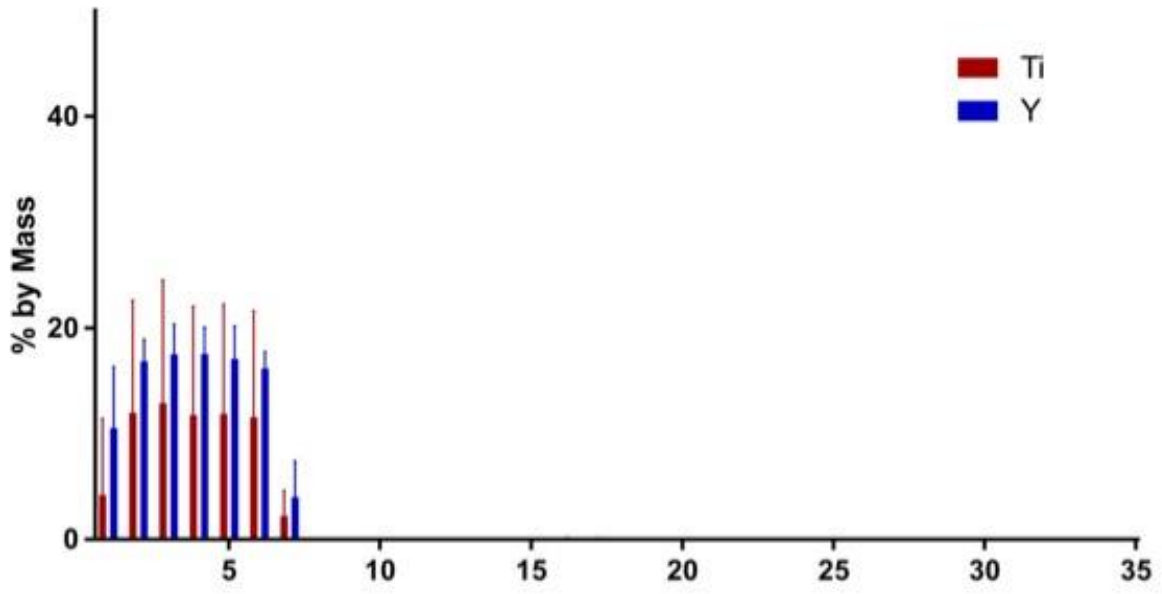

Figure 3-4 ICP-MS percent by mass elution profile for Y and Ti for each fraction

^{89}Zr Labeling and Specific Activity: Labeling studies performed using DFO-panitumumab showed 97±8% labeling for ^{89}Zr-IDA and 99.8±0.6% ^{89}Zr-oxalate ($p = 0.2381$). When the labeling reaction was challenged with DTPA, the ^{89}Zr-IDA method labeled antibody had 94±8% labeling remain and the ^{89}Zr-oxalate method labeled antibody had 96±6% remain ($p = 0.3885$). The ^{89}Zr-IDA compared to ^{89}Zr-oxalate show no significant difference between the labeling even when challenged with DTPA. This shows that this alternative method results in a high-quality product suitable for radiolabeling studies. Using the standard method to determine the ESA of ^{89}Zr-IDA resulted in an ESA of 24±3 mCi/μmol. The relatively low ESA can be attributed to the small batches of activity studied thus far. ESA values in literature typically range from 108±7 mCi/μmol reported by Queern et al. to 470-1195 mCi/μmol reported by Holland et al. [1, 6]. It is likely that scaling up the batch size of activity will result in a higher ESA.

3.4 Conclusions

Herein, we evaluated the low-level activity separations of ^{89}Zr from Y to evaluate the suitability of pCST resin using an IDA eluant as a new purification strategy. This method may provide ease in automating the separation system and potentially eliminates the need to remove the oxalate chelator before injection. Our work shows reproducible results in these low-level separations. The test labeling of antibodies with the recovered ^{89}Zr showed that DFO conjugated antibodies can be successfully labeled with comparable yields to current methods. Overall, this method shows potential for an alternative method for the separation of ^{89}Zr from Y.

3.5 Acknowledgments

This work was supported by U. S. Department of Energy, Office of Science, Nuclear Physics (grant number ST-50-01-020) and by the Department of Radiology at University of Alabama at Birmingham. The authors would like to thank the UAB Cyclotron facility for the production of the ^{89}Zr for all radioactive studies.

3.6 References

1. Holland, J. P.; Sheh, Y.; Lewis, J. S., Standardized methods for the production of high specific-activity zirconium-89. *Nucl Med Biol* **2009,** *36* (7), 729-39.
2. Sadeghi, M. E., M.; Bakhtiari, M., Accelerator production of the positron emitter zirconium-89. *Annals of Nuclear Energy* **2012,** *41*, 97-103.
3. Fischer, G.; Seibold, U.; Schirrmacher, R.; Wangler, B.; Wangler, C., (89)Zr, a radiometal nuclide with high potential for molecular imaging with PET: chemistry, applications and remaining challenges. *Molecules* **2013,** *18* (6), 6469-90.
4. Marquez, B. V.; Ikotun, O. F.; Zheleznyak, A.; Wright, B.; Hari-Raj, A.; Pierce, R. A.; Lapi, S. E., Evaluation of (89)Zr-pertuzumab in Breast cancer xenografts. *Mol Pharm* **2014,** *11* (11), 3988-95.

5. Severin, G. W.; Engle, J. W.; Barnhart, T. E.; Nickles, R. J., 89Zr radiochemistry for positron emission tomography. *Med Chem* **2011,** *7* (5), 389-94.
6. Queern, S. L.; Aweda, T. A.; Massicano, A. V. F.; Clanton, N. A.; El Sayed, R.; Sader, J. A.; Zyuzin, A.; Lapi, S. E., Production of Zr-89 using sputtered yttrium coin targets. *Nucl Med Biol* **2017,** *50*, 11-16.
7. Wooten, A. L. M., E.; Schweitzer, G. D.; Lawrence, L. A.; Mebrahtu, E.; Lewis, B. C.; Lapi, S. E., Routine Production of ^{89}Zr Using Automated Module. *Appl. Sci.* **2013,** *3*, 593-613.
8. Kasbollah, A.; Eu, P.; Cowell, S.; Deb, P., Review on production of 89Zr in a medical cyclotron for PET radiopharmaceuticals. *J Nucl Med Technol* **2013,** *41* (1), 35-41.
9. Clearfield, A.; Medvedev, D. G.; Kerlegon, S.; Bosser, T.; Burns, J. D.; Jackson, M., Rates of Exchange of Cs+ and Sr2+ for Poorly Crystalline Sodium Titanium Silicate (CST) in Nuclear Waste Systems. *Solvent Extraction and Ion Exchange* **2012,** *30* (3), 229-243.
10. Chitra, S.; Viswanathan, S.; Rao, S. V. S., Uptake of cesium and strontium by crystalline silicotitanates from radioactive wastes. *J. Radioanal Nucl Chem* **2011,** *287* (3), 955-960.
11. Rhodes, G., Chapter 3 - Protein Crystals. In *Crystallography Made Crystal Clear (Third Edition)*, Rhodes, G., Ed. Academic Press: Burlington, 2006; pp 31-47.
12. Zheng, Z.; Philip, C. V.; Anthony, R. G.; Krumhansl, J. L.; Trudell, D. E.; Miller, J. E., Ion Exchange of Group I Metals by Hydrous Cyrstalline Silicotitanates. *Ind. Eng. Chem. Res.* **1996,** *35*, 4246-56.
13. Markowicz-Piasecka, M.; Mikiciuk-Olasik, E.; Sikora, J., Stability of erythrocyte membrane and overall hemostasis potential - A biocompatibility study of mebrofenin and other iminodiacetic acid derivatives. *Pharmacol Rep* **2015,** *67* (6), 1230-9.
14. Vosjan, M. J.; Perk, L. R.; Visser, G. W.; Budde, M.; Jurek, P.; Kiefer, G. E.; van Dongen, G. A., Conjugation and radiolabeling of monoclonal antibodies with zirconium-89 for PET imaging using the bifunctional chelate p-isothiocyanatobenzyl-desferrioxamine. *Nat Protoc* **2010,** *5* (4), 739-43.

Chapter 4

Radiolabeled nano-hydroxyapatite as a new platform for PET imaging agents

[This work has been submitted previously as "Radiolabeled nano-hydroxyapatite as a new platform for PET imaging agents," Stacy L Queern, Tolulope A. Aweda, Nicholas A. Clanton, Alan R. Ketring, Heather M. Hennkens, and Suzanne E. Lapi, *Molecular Imaging.* **2018**]

4.1 Introduction

There is a large breadth of uses for nanoparticles, such as targeted drug delivery, photoablation therapy and bioimaging [1-2]. The use of nanoparticles in the medical field has growing interest due to their many advantageous characteristics, including availability in many shapes, sizes and with varying surface characteristics [3-4]. Nanoparticles offer a large surface to volume ratio that makes them potential candidates for targeted molecular imaging and therapy [5].

Zirconium-89 (^{89}Zr) is commonly used in the research arena for positron emission tomography (PET) imaging of radiolabeled monoclonal antibodies. This is in part due to its long half-life (78.4 h), which is compatible with the biological half-lives of antibodies and nanoparticles [6-8]. It is well known that free ^{89}Zr is a bone seeker, which means that if the ^{89}Zr decomplexes from the chelating agent, it will accumulate in the bone, [7, 9]. There are several radionuclides that are considered bone seekers due to their high affinity for bone, including fluorine-18 (^{18}F), samarium-153 (^{153}Sm), and ^{89}Zr. These bone seekers have great potential for PET imaging or cancer therapy, but if they are not stably complexed or otherwise attached to the targeting vector in vivo, they may accumulate in the bone [9]. Although bone uptake of ^{89}Zr is not commonly seen in human subjects, it remains a problem in preclinical studies and may cause difficulty in translating dosimetry from animal models to humans [7].

Bone is made of a matrix of compounds, the main component of which is hydroxyapatite (HAp), ($HCa_5O_{13}P_3$) [10-12]. Current uses of HAp in the dental and medical fields include dental enamel replacement, bone grafting and drug delivery [13-15]. Although HAp is well known, little work has been done with nano-hydroxyapatite (nHAp) as a radiolabeled PET tracer. In one study, Zheng et al. successfully labeled nHAp with ^{18}F to determine biodistribution and

pharmacokinetics of ^{18}F-nHAp using PET imaging and showed that ^{18}F-nHAp was retained in the body for at least 160 minutes [16]. The long circulation period of nHAp means that longer-lived radionuclides are required for the development of nHAp-based tumor targeting agents.

The goal of our research is to exploit the natural affinity of ^{89}Zr and other radionuclides for bone to synthesize radiolabeled nHAp particles. Development of rapid radiochemistry could enable a new class of imaging agents with kit-like formulations. The use of nHAp provides substantial surface area for radiolabeling and the potential for attachment of targeting moieties and drug loading. We investigated labeling efficiencies of several radionuclides for nHAp and the stability of the radiolabeled products over two half-lives. Analyses and comparisons of the size and shape of nHAp and the role of these parameters on labeling, stability and biodistribution in mice were assessed.

4.2 Methods

Materials

^{89}Zr, ^{18}F, and ^{55}Co were produced by the University of Alabama at Birmingham (UAB) cyclotron facility (Birmingham, AL) [17-18], ^{64}Cu was purchased from Washington University School of Medicine (WUSM) cyclotron facility (St. Louis, MO) and ^{153}Sm was obtained from the University of Missouri Research Reactor (MURR) (Columbia, MO). Sphere-shaped HAp nanopowder with a reported particle size of <200 nm was purchased from Sigma Aldrich (St. Louis, MO). Needle-shaped HAp particles with a reported average particle length of 20 nm were purchased from M K Impex Corp. (Mississauga, Ontario, Canada). All other chemicals were purchased from Fisher Scientific.

Particle Characterization

Transmission Electron Microscopy (TEM) was performed at either Washington University in St. Louis (WUSTL) Nano Research Facility with a FEI Tecnai G^2 Spirit or at UAB High Resolution Imaging Facility with a FEI Tecnai T12 Spirit. All samples were suspended in methanol and placed on a carbon support film with 200 mesh copper.

Radiolabeling and Stability Studies

All labeling studies were conducted with 50 μg of nHAp, either sphere-shaped or needle-shaped, dispersed in 300 μL of 1x PBS. The pH of all radioisotope solutions was adjusted to 7.1 using 1 M HEPES (pH=7.1) as a buffer and 2 M NaOH and/or 1 M HCl for pH adjustments. A 50 μCi (1 – 110 μL) aliquot of the radionuclide solution was added to the nHAp solution and then incubated at 37° C with agitation for several time points up to 60 minutes. The samples were centrifuged at 15,000 rpm for 2 minutes and the supernatant was removed. The samples were washed three times with 1 mL of 1x PBS, centrifuged, supernatant removed, and the radioactivity associated with the nHAp was measured with a CRC-25 dose calibrator (Capintec, Inc., NJ). Determination of the maximum amount of radioactivity adhered to the nHAp was investigated using variable activity (40 – 200 μCi) added to the 50 μg of nHAp mass. Ten-minute labeling intervals were studied. ^{64}Cu-nHAp and ^{55}Co-nHAp were used as controls, since these isotopes are not bone seekers.

All stability studies were completed using the highest achieved specific activity radiolabeled nHAp over the course of two half-lives of the radioisotope in 300 μL of either fetal bovine serum (FBS) or human serum (HS). The ^{64}Cu-nHAp and ^{55}Co-nHAp were used as controls for the FBS studies, and ^{64}Cu-nHAp was used as a control for the HS study. In order to determine the amount

of radioactivity still associated with the particles, the particles were centrifuged after two half-lives at 15,000 rpm for 2 minutes, the serum was removed, and the activity associated with the pellet was measured.

Biodistribution Studies

All animal studies were conducted under a protocol approved by the Institutional Animal Care and Use Committee (IACUC) at the University of Alabama at Birmingham. Biodistribution studies were carried out for both nHAp morphologies in normal mice (32-38 days old, male, CD-1 IGS, n=4). 50 µCi of ^{89}Zr-nHAp in 100 µL of 0.9% sodium chloride solution was injected via tail vein. Animals were sacrificed via cervical dislocation at 4 hours, 24 hours, 72 hours and 7 days post injection, and organs were harvested and analyzed for radioactivity using a 2480 Wizard 2 Gamma Counter (Perkin Elmer, MA). Radioactivity associated with each organ is expressed as percentage of injected dose per gram of organ (%ID/g).

Statistical Analysis

All data is reported as mean ± standard deviation and was calculated using *Microsoft Excel* version 16. All p-values were determined using *Prism* version 7 one-way ANOVA multiple comparison with 95% confidence where $p < 0.05$ was considered significant.

4.3 Results

Particle Characterization

TEM of the two types of nHAp confirmed the morphology of each and allowed determination of average particle size. Figure 4-1 shows an image for each of the morphologies. Both morphologies illustrated extremely variable particle sizes. By TEM, the sphere-shaped nHAps

were found to have a range of 13 nm – 1149 nm, with an average particle diameter size of 206 nm (n=109). The needle-shaped nHAp ranged in length from 9 nm – 357 nm, with an average length of 76 nm (n=76) and ranged in width from 6 nm – 51 nm, with an average width of 19 nm (n=53).

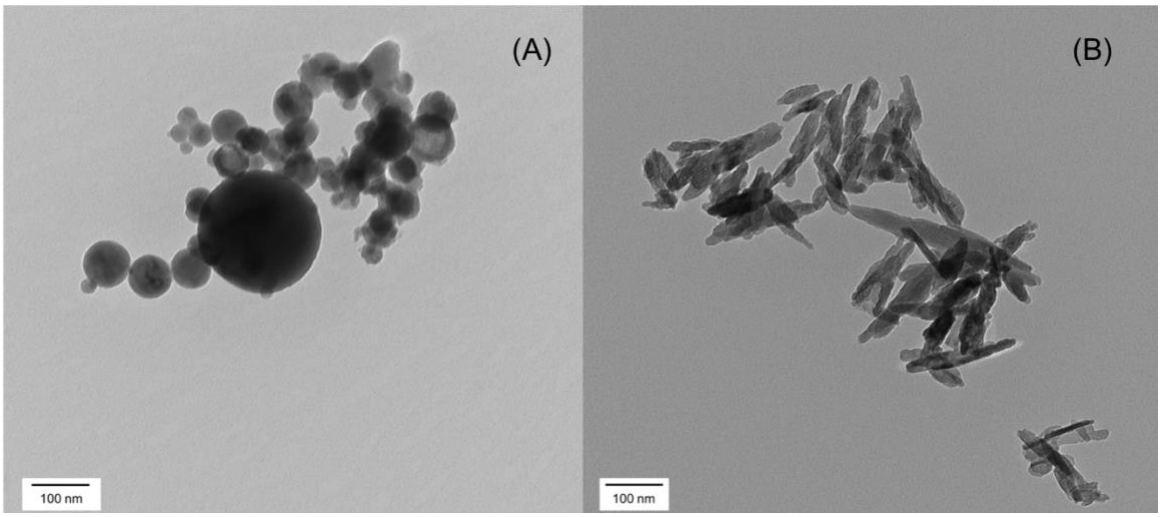

Figure 4-1 TEM images of sphere-shaped particles (A) and needle-shaped particles (B) Radiolabeling and Stability Studies

nHAp was radiolabeled with ^{89}Zr, ^{18}F, ^{153}Sm, ^{64}Cu, and ^{55}Co and the stability of the adhesion of each radionuclide to nHAp was assessed. The time needed to incorporate maximum radioactivity on the nHAp, maximum specific activity achievable, and stability in FBS and HS for two half-lives were determined for each radionuclide-nHAp. A summary of this data is shown in Table 4-1.

Table 4-1 Labeling and Stability of Radiolabeled Sphere- vs. Needle-Shaped nHAp

Radionuclide	Half-life (h)	Minimal Time for Maximum Labeling (min)	Maximum Specific Activity (μCi/μg)	% Intact After Two Half-lives (FBS)†	% Intact After Two Half-lives (HS)†
^{89}Zr	78.41	10	Sphere: 1.31±0.19 Needle: 2.8±0.3	100±3 98.2±1.2	91±2 92±2
^{18}F	1.83	5	Sphere: 27±3 Needle: 38.4±0.2	86.9±1.3 75.5±1.6	NP*
^{153}Sm	46.28	10	Sphere: 11.75±0.18 Needle: 11.0±0.3	91.4±1.1 90.4±1.1	NP*
^{64}Cu	12.70	15	Sphere: 12.41±0.02 Needle: 14.27±0.13	64±2 23.74±0.10	56±3 35±2
^{55}Co	17.53	30	Sphere: 0.76±0.09 Needle: 1.49±0.11	55±5 44±3	NP*

†n=3; *NP - not performed

Figure 4-2 shows the radiolabeling yields at various labeling times for the radionuclides studied. Over 90% labeling was achieved for all bone seeking radionuclides in less than 10 minutes, with relatively low radiolabeling yields achieved for the non-bone seeker, ^{55}Co, as expected.

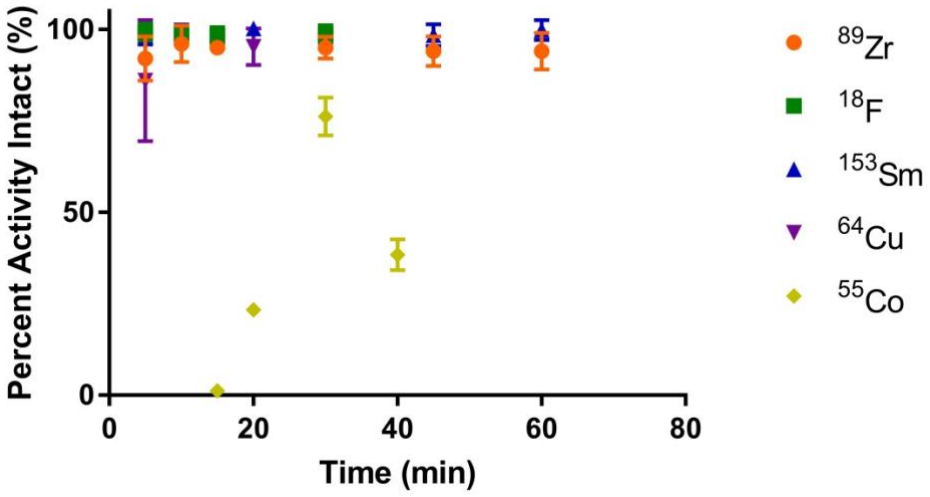

Figure 4-2 Radiolabeling trends of nHAp for radionuclides studied

Tables 4-1 and 4-2 show the significant difference between the stabilities of the sphere- and needle-shaped particles after two half-lives, where the radiolabeled sphere-shaped particles were more stable than the needle-shaped particles. Furthermore, the data shows that the stability trend for both morphologies was ^{89}Zr > ^{153}Sm > ^{18}F > ^{64}Cu > ^{55}Co. ^{89}Zr-nHAp and ^{64}Cu-nHAp were further tested for stability in HS for two half-lives. The data in Table 4-1 shows, as expected, the ^{89}Zr radiolabeled sphere-shaped and needle-shaped particles are stable in HS, while the ^{64}Cu particles are less stable. The ^{89}Zr particles have similar stability in both HS and FBS.

Table 4-2 Statistical Data (p-values) for the Stability of the Labeled nHAp in FBS

sphere needle	^{89}Zr	^{18}F	^{153}Sm	^{64}Cu	^{55}Co
^{89}Zr	>0.9999	<0.0001	0.0058	<0.0001	<0.0001
^{18}F	<0.0001	<0.0001	0.0188	<0.0001	<0.0001
^{153}Sm	0.0008	<0.0001	>0.9999	<0.0001	<0.0001
^{64}Cu	<0.0001	<0.0001	<0.0001	<0.0001	0.0005
^{55}Co	<0.0001	<0.0001	<0.0001	<0.0001	<0.0001

*Black font represents p-values of sphere-shaped particles relative to other sphere-shaped particles, red font represents p-values of needle-shaped particles relative to other needle-shaped particles, and blue font represents p-values of sphere-shaped particles relative to needle-shaped particles for the same radionuclide.

The biodistributions in normal mice for both ^{89}Zr-nHAp morphologies are shown in Figure 4-3. These data show less than 5% bone uptake, with uptake in the lung and retention in the liver and spleen (likely due to particle size). The needle-shaped nHAp had less uptake in the bone ($p < 0.003$), lungs ($p < 0.01$) and kidneys ($p < 0.001$) compared to the sphere-shaped nHAp at seven days. The biodistribution shows the smaller particles (needle-shaped) have less uptake in bone, kidney and lung, which implies that smaller particles may make better tumor targeting agents [3].

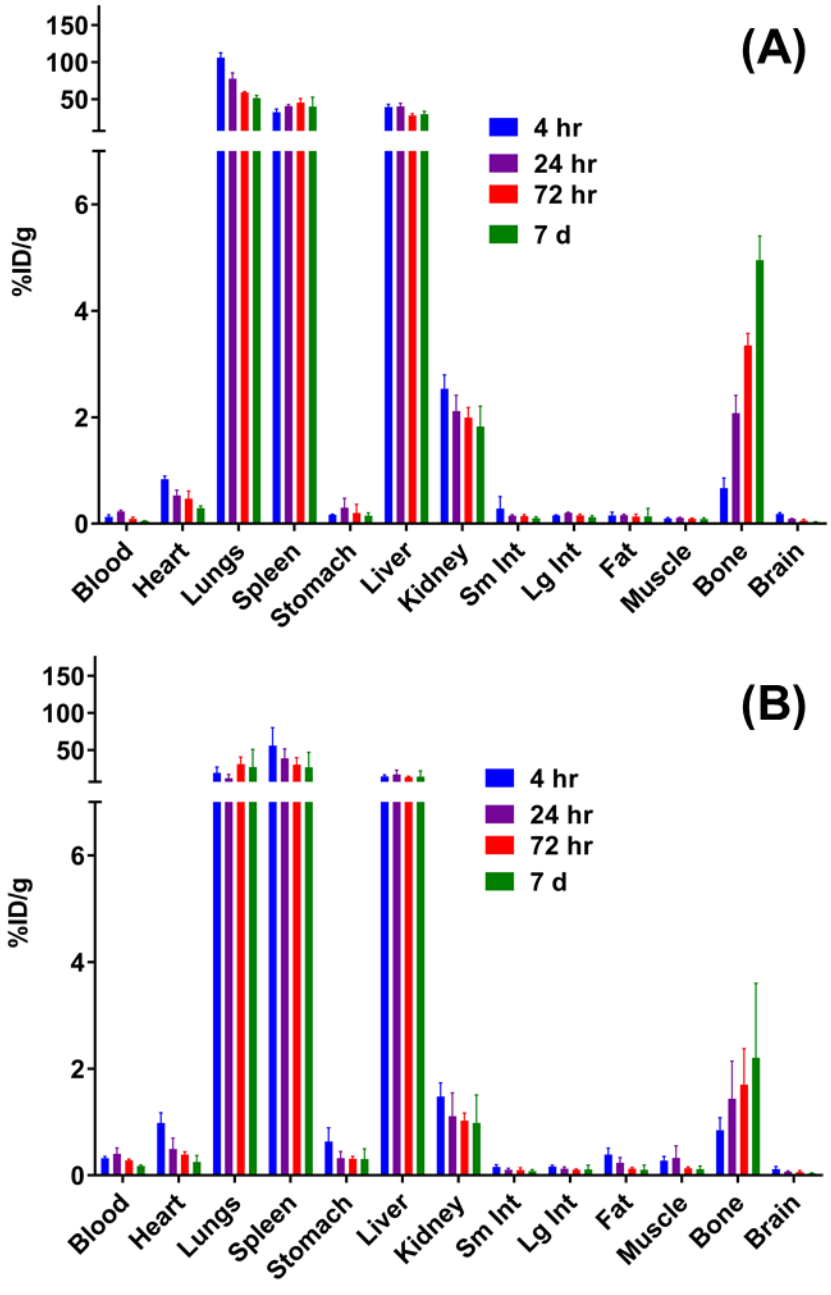

Figure 4-3 (A) Biodistribution for sphere-shaped ^{89}Zr-nHAp and (B) biodistribution for needle-shaped ^{89}Zr-nHAp

4.4 Discussion

The goal of our research was to exploit the natural affinity of ^{89}Zr and other radionuclides for bone to develop a rapid labeling technique for nHAp. In order to evaluate the potential of nHAp as a new class of imaging agents, we examined the labeling efficiencies and stability of adsorption to nHAp for several radionuclides. The role of the size and shape of nHAp on labeling and stability for ^{89}Zr, ^{18}F, ^{153}Sm, ^{64}Cu and ^{55}Co was investigated. The two different ^{89}Zr-nHAp morphologies were used for biodistribution studies in normal mice.

The TEM data showed the morphology and size of both the commercially obtained sphere- and needle-shaped nHAp. Both the sphere- and needle-shaped particles have a large variability from the reported average particle size. The sphere-shaped particles show greater deviation in particle size, and Figure 4-1A clearly shows that the size of these nHAp particles is not uniform. The needle-shaped particles are significantly larger than the reported value but are smaller relative to the sphere-shaped nHAp.

The labeling data show that radiolabeling of nHAp with ^{18}F proceeded rapidly (5 minutes), which is consistent with literature data [16]. Higher specific activity was achieved with the needle-shaped nHAp for all radionuclides except ^{153}Sm, for which the specific activities were approximately the same. This is expected due to the increased surface to volume ratio for smaller particles. The stability data show that (as expected) particles radiolabeled with known bone seekers have higher stability than the non-bone seekers, where ^{89}Zr and ^{153}Sm exhibited the best stability with > 98.2% and > 90.4% intact after two half-lives (156.8 h and 92.6 h), respectively, for both nHAp morphologies. It is possible that ^{18}F showed less stability compared to ^{89}Zr and ^{153}Sm because it is a non-metal with a negative charge (F^-) compared to $^{89}Zr^{4+}$ and $^{153}Sm^{3+}$,

which are transition metals with positive charges. This positive charge may offer additional stability due to ionic interactions between the metals and the negatively-charged hydroxide (OH^-) groups on the surface of the nanoparticles. However, the ^{18}F can only adhere via covalent or hydrogen bonding, both of which are weaker than ionic bonding. For ^{18}F, ^{64}Cu, and ^{55}Co, the radiolabeled needle-shaped nHAp showed lower stability than the sphere-shaped nHAp with p-values less than 0.01. This was further confirmed in the ^{64}Cu-nHAP stability experiments using human serum. Sphere- and needle-shaped ^{89}Zr-nHAp were equally stable, whereas ^{64}Cu-nHAp and ^{55}Co-nHAp were less stable overall and the stabilities were less consistent between particle morphologies. This trend for ^{64}Cu-nHAp and ^{55}Co-nHAp is expected, since they are not bone seekers.

The biodistributions for both sphere-shaped and needle-shaped nHAp showed low ^{89}Zr uptake in the bone (<5% ID/g), with localization in the lungs, liver and spleen. In comparison, Marquez et al. reported biodistributions with upwards of 20% ID/g uptake in the bone with ^{89}Zr-DFO-pertuzumab, a monoclonal antibody that targets HER2 receptors [19]. The bone uptake can be attributed to the likely decomplexation of the ^{89}Zr from the ^{89}Zr-DFO. Our work clearly demonstrates significantly less uptake in the bone, which supports low desorption of the ^{89}Zr from ^{89}Zr-nHAp in vivo. Overall, the data show that this strategy has potential for the development of imaging and therapy agents with bone seeking radionuclides using nHAp.

4.5 Conclusions

Our studies illustrate how the high affinity of ^{89}Zr for nHAp may aid in the development of new imaging agents. Overall, ^{89}Zr-nHAp was shown to be a good candidate for the development of new targeted PET imaging agents. The particles are easily labeled with bone seeking

radionuclides and have high in vitro stability with little bone uptake in vivo. Our future work will include the modification of nHAp to include tumor targeting agents and the assessment of the effect these modifications have on labeling, in vitro stability and in vivo pharmacokinetics.

4.6 Acknowledgments

The authors of this article would like to thank the Department of Radiology at the University of Alabama at Birmingham (UAB) for funding, the UAB Cyclotron Facility for the production of ^{89}Zr, ^{18}F, and ^{55}Co, the University of Missouri Research Reactor (MURR) for the production of ^{153}Sm, and the UAB Small Animal Imaging Facility for biodistribution studies. The UAB Small Animal Imaging Facility is supported through the UAB Comprehensive Cancer Center P30CA013148 grant from NIH.

4.7 References

1. Murthy, S. K., Nanoparticles in modern medicine: State of the art and future challenges. *Int J Nanomedicine* **2007,** *2* (2), 129-41.
2. Wu, C. C.; Yang, Y. C.; Hsu, Y. T.; Wu, T. C.; Hung, C. F.; Huang, J. T.; Chang, C. L., Nanoparticle-induced intraperitoneal hyperthermia and targeted photoablation in treating ovarian cancer. *Oncotarget* **2015,** *6* (29), 26861-75.
3. Hoshyar, N.; Gray, S.; Han, H.; Bao, G., The effect of nanoparticle size on in vivo pharmacokinetics and cellular interaction. *Nanomedicine (Lond)* **2016,** *11* (6), 673-92.
4. Salata, O., Applications of nanoparticles in biology and medicine. *J Nanobiotechnology* **2004,** *2* (1), 3.
5. McNamara, K., Nanoparticles in biomedical applications. *Advances in Physics* **2017,** *2* (1), 54-88.
6. Holland, J. P.; Sheh, Y.; Lewis, J. S., Standardized methods for the production of high specific-activity zirconium-89. *Nucl Med Biol* **2009,** *36* (7), 729-39.
7. Deri, M. A.; Zeglis, B. M.; Francesconi, L. C.; Lewis, J. S., PET imaging with ^{89}Zr: from radiochemistry to the clinic. *Nucl Med Biol* **2013,** *40* (1), 3-14.
8. Van Dongen, G. A. M. S.; Visser, G. W. M.; Lub-de Hooge, M. N.; de Vries, E. G.; Perk, L. R., Immuno-PET: A navigator in monoclonal antibody development and applications. *Oncologist* **2007,** *12*, 1379-89.

9. Abou, D. S.; Ku, T.; Smith-Jones, P. M., In vivo biodistribution and accumulation of (89)Zr in mice. *Nucl Med Biol* **2011,** *38* (5), 675-81.
10. Zhou, H.; Lee, J., Nanoscale hydroxyapatite particles for bone tissue engineering. *Acta Biomater* **2011,** *7* (7), 2769-81.
11. Kojima, C.; Watanabe, K., Adsorption and desorption of bioactive proteins on hydroxyapatite for protein delivery systems. *J Drug Deliv* **2012,** *2012*, 932461.
12. Matsumoto, T.; Okazaki, M.; Inoue, M.; Hamada, Y.; Taira, M.; Takahashi, J., Crystallinity and solubility characteristics of hydroxyapatite adsorbed amino acid. *Biomaterials* **2002,** *23* (10), 2241-7.
13. Murugan, R., Aqueous mediated synthesis of bioresorbable nanocrystalline hydroxyapatite. *Journal of Crystal Growth* **2005,** *274*, 209-13.
14. Hao, X.; Hu, X.; Zhang, C.; Chen, S.; Li, Z.; Yang, X.; Liu, H.; Jia, G.; Liu, D.; Ge, K.; Liang, X. J.; Zhang, J., Hybrid mesoporous silica-based drug carrier nanostructures with improved degradability by hydroxyapatite. *ACS Nano* **2015,** *9* (10), 9614-25.
15. Sammons, R., Biological responses to hydroxyapatite. In *Hydroxyapatite (HAp) for Biomedical Applications*, Mucalo, M. R., Ed. Woodhead Publishing: Sawston, Cambridge, UK, 2015; pp 53-83.
16. Zheng, J.; Zhou, W., In vivo imaging of nano-hydroxyapatite biodistribution using positron emission tomography imaging. *Chem. Lett.* **2012,** *41*, 1606-07.
17. Queern, S. L.; Aweda, T. A.; Massicano, A. V. F.; Clanton, N. A.; El Sayed, R.; Sader, J. A.; Zyuzin, A.; Lapi, S. E., Production of (89)Zr using sputtered yttrium coin targets *Nucl Med Biol* **2017,** *50*, 11-16.
18. Mastren, T.; Marquez, B. V.; Sultan, D. E.; Bollinger, E.; Eisenbeis, P.; Voller, T.; Lapi, S. E., Cyclotron production of high-specific activity (55)Co and in vivo evaluation of the stability of (55)Co metal-chelate-peptide complexes. *Mol Imaging* **2015,** *14* (10), 526-33.
19. Marquez, B. V.; Ikotun, O. F.; Zheleznyak, A.; Wright, B.; Hari-Raj, A.; Pierce, R. A.; Lapi, S. E., Evaluation of (89)Zr-pertuzumab in breast cancer xenografts. *Mol Pharm* **2014,** *11* (11), 3988-95.

Chapter 5

^{89}Zr-nano-hydroxyapatite modified with phospha-TOC as a targeted PET agent

[This work has been presented previously at the ISRS 2017 meeting as "^{89}Zr-nanohydroxyapatite-phospha-TOC as a new PET imaging agent" Stacy L Queern, Adriana V. F. Massicano, Jennifer L. Burkemper, Nicholas A. Clanton, and Suzanne E. Lapi, **May 2018**]

5.1 Introduction

Nanoparticles are used in drug delivery and therapy in the medical field because they offer unique properties due their size and surface characteristics [1-2]. Currently there are many types of nanoparticles being used in biomedical research as the variety in the morphology results in an expansive research toolbox. For example, the large surface to volume ratio of nanoparticles provides a platform for targeted imaging and/or therapy [3].

Zirconium-89 (^{89}Zr) has a half-life of 3.27 days which is compatible with the biological half-life of antibodies and nanoparticles [4-6]. This characteristic has made this radionuclide of significant interest in the molecular imaging field. An additional important feature to note is that free ^{89}Zr is a bone seeker. This means that ^{89}Zr has a high affinity for bone, thus if decomplexes from the compound it will accumulate in the bone [7-8]. Although this is not frequently seen in human studies, it may cause issues with preclinical experiments and translation of dosimetry to clinical trials [5, 7].

One way to label nanoparticles with ^{89}Zr was been discussed in our previous work (Chapter 4) using nanohydroxyapatite (nHAp). nHAp is the main component in the bone matrix [9-11] and thus ^{89}Zr has a natural high affinity for nHAp. Our previous studies have shown rapid labeling and high in vitro stability with minimum release and bone uptake in vivo. Modification of nHAp would allow for targeted molecular imaging or therapy. As a proof of concept, the peptide, [Tyr^3]octreotide (TOC) was used to modify nHAp in order target somatostatin receptors, namely SSTR2 receptors, which are over-expressed on neuroendocrine tumors [12-14]

The aim of this work was to perform a rapid modification of nHAp using an analog of TOC to target neuroendocrine tumors. Herein, we discuss the preparation of co-precipitated ^{89}Zr with

nHAp and the modification of the nHAp with phospha-TOC. The binding of the modified ^{89}Zr-nHAp to rat pancreatic tumor cells, AR42J, that overexpress SSTR2 and distribution in immunodeficient mice with tumor xenografts from the same cell line were examined to investigate specific targeting of the modified nHAp.

5.2 Methods

Materials

^{89}Zr was produced by the Cyclotron Facility at University of Alabama at Birmingham [4]. [Tyr3]-octreotide (TOC) was obtained from CPC Scientific (Sunnyvale, CA) and phospha-TOC ({d-PHE}CY{d-TRP}KTC{pTHR}), an analog of TOC, was obtained from GenScript (Piscataway, NJ). All other chemical reagents and supplies were purchased from Fisher Scientific (Pittsburgh,PA) or Sigma (St. Louis, MO).

Co-precipitation preparation of ^{89}Zr-nHAp

A solution of 2.5 ml of 0.5 M calcium chloride ($CaCl_2$), 2.5 ml of 0.1 M trisodium citrate ($Na_3C_6H_5O_7$) and approximately 100 μL of ^{89}Zr were mixed and allowed to react for 30 minutes on a vortexer. A second solution of 1.25 mL 0.03 M ammonium hydrogen phosphate ($(NH_4)_2HPO_4$) and 0.5 mL of ammonium hydroxide (NH_4OH) was added dropwise to the first solution then pH adjusted to pH 9 using concentrated nitric acid. The reaction was allowed to proceed for another 30 minutes before the final product was removed via centrifugation and washed three times with 18Ω milli-Q water removing water with centrifugation each time [15].

Transmission Electron Microscopy (TEM) was performed to characterize the nHAp at UAB High Resolution Imaging Facility with a FEI Tecnai T12 Spirit. All samples were suspended in methanol and a 1 μL aliquot was spotted on a carbon support film with 200 mesh copper.

Stability studies were completed using approximately 200 μCi of co-precipitated ^{89}Zr-nHAp over the course of 7 d in 300 μL of fetal bovine serum (FBS). After incubation, the particles were centrifuged at 15,000 rpm for 2 minutes, the serum was removed, and the activity associated with the pellet was measured on a Capintec CRC-25 dose calibrator (Florham Park, NJ).

Modification of ^{89}Zr-nHAp with phospha-TOC

For modification of ^{89}Zr-nHAp, 2 mg of phospha-TOC was dissolved in water and introduced to the reaction vessel with ~300 μg (~1 mCi) of ^{89}Zr-nHAp. The reaction was allowed to proceed for one hour at room temperature on a thermoshaker. The proposed reaction mechanism is given in Figure 5-1. The product was removed using centrifugation and washed several times with PBS. Once the ^{89}Zr had decayed ten half-lives, the washes and final product were analyzed on Agilent 6530 Quadrupole Time-of-Flight (QTOF) LC/MS (Santa Clara, CA). A 500 μL aliquot of each wash was analyzed without any further dilutions. The final product was dissolved in 100 μL chloroform and a 10 μL sample was diluted to 500 μL of 50% acetonitrile with 0.1% formic acid and then analyzed on the QTOF.

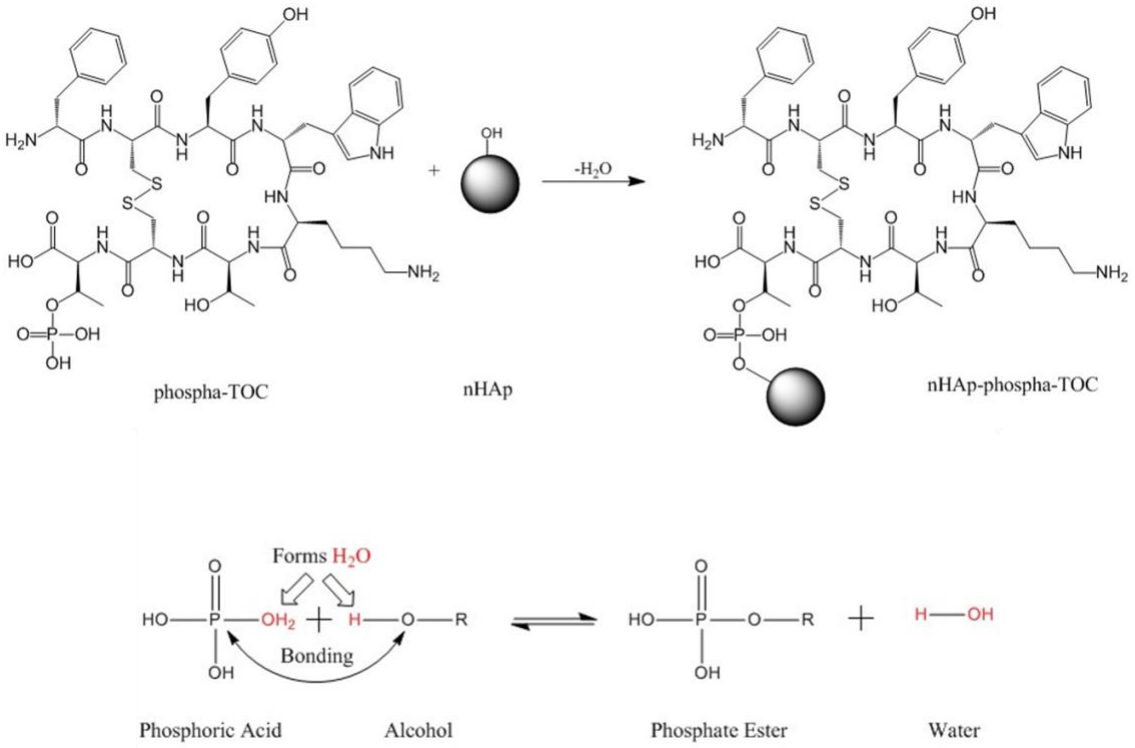

Figure 5-1 Modification of nHAp with phospha-TOC

Cell Studies with ^{89}Zr-nHAp-phosph-TOC

The specific targeting of ^{89}Zr-nHAp-phospha-TOC was tested on AR42J cell lines which have an overexpression of somatostatin receptor 2 (SSTR2) [13,16]. Approximately 2 x 10^6 million of cells were plated per well on 12-well plates. 0.5 μCi (1.3 μg) ^{89}Zr-nHAp-phospha-TOC was introduced to all wells where 4 of the wells were designated for each of the following: non-blocking, blocking and bare nanoparticles (no peptide). The blocking study used ~380 μg TOC to block the SSTR2 receptors to show that specific binding was occurring. The cells were incubated at 37^{o}C in a 5% CO_2 atmosphere for 2 hours. The cells were washed with cold PBS two times and then trypsinized for 5 minutes. The trypsin was neutralized with an equivalent

volume of cell media and then the cells were collected. The collected cells and each wash were analyzed for radioactivity using a 2480 Wizard 2 Gamma Counter (Perkin Elmer, MA).

Cells were counted directly after gamma analysis. A 20 µL aliquot of the cell sample was placed on a plastic cell counting chamber and counted in a Nexcelom Cellometer Auto T4 (Lawrence, MA) using Cellometer Auto Center version 3.3.7.1. Bovine serum albumin (BSA) protein assay was completed following the cell counts. BSA calibration standards for the protein bioassay were of 2000, 1000, 500, 250, 125, 62.5, 31.25, and 0 µg/mL in concentration. All samples had a 5-fold dilution in the same matrix. 10 µL of each standard and sample was aliquoted in triplicate into a 96-well plate.100 µL of bicinchoninic acid color agent was added to each well and incubated for 30 minutes at 37^{o}C. The plate was analyzed on BioTek Synergy Mx plate reader (Winooski, VT) using Gen5 All-in-One version 2.09 software.

Animal Studies with ^{89}Zr-nHAp-phospha-TOC

All animal studies were conducted under a protocol approved by the Institutional Animal Care and Use Committee (IACUC) at the University of Alabama at Birmingham. Seven-week-old female athymic nude mice were anesthetized and implanted with approximately 3 x 10^6 AR42J rat pancreatic tumor cells on their right hind quarters. The tumor was allowed to grow for 10-14 days before imaging and biodistribution studies were performed.

Each mouse was injected with approximately 100 µCi (~200 µg) of ^{89}Zr-nHAp-phospha-TOC in 100 µL of 0.9% sodium chloride solution via tail vein. PET imaging was conducted using a Sofie BioSciences GNEXT PET/CT scanner (Dulles, VA) at 4, 24, and 72 h post-injection with post-imaging biodistributions to examine the uptake of ^{89}Zr-nHAp-phospha-TOC over time. To determine if specific uptake was occurring, a blocking study was performed using TOC to block

the SSTR2 receptors on the tumors. The blocking PET imaging study was completed at 24 h post-injection with post-imaging biodistributions using 100 µg of TOC co-injected with the 100 µCi of ^{89}Zr-nHAp-phospha-TOC in 100 µL of 0.9% sodium chloride solution via tail vein [13]. All images were analyzed using Invicro VivoQuant version 3.5 software (Boston, MA).

For the post-imaging biodistribution studies, the mice were sacrificed via cervical dislocation at 4, 24, 72 hours post-injection, and organs were harvested and analyzed for radioactivity using a 2480 Wizard 2 Gamma Counter (Perkin Elmer, MA). Radioactivity associated with each organ is expressed as percentage of injected dose per gram of organ (%ID/g).

Statistical Analysis

Prism version 7 was used to determine the p-values using one-way ANOVA multiple comparison with 95% confidence where $p < 0.05$ was considered significant.

5.3 Results and Discussion

Co-precipitation preparation of ^{89}Zr-nHAp

The production of the co-precipitated ^{89}Zr-nHAp resulted in a 98.7±1.3% radiochemical yield which illustrates that the coprecipitation labeling is highly efficient. Figure 5-2 shows an image of the co-precipitated ^{89}Zr-nHAp. The TEM image showed irregular spherical particle shapes that measure an average of 64.8 nm (n=108) with a range in particle size of 8.9 – 175 nm. The average particle size and range of the co-precipitated ^{89}Zr-nHAp compared to the needle- and sphere-shaped particles showed smaller average particle sizes as well as a narrower range.

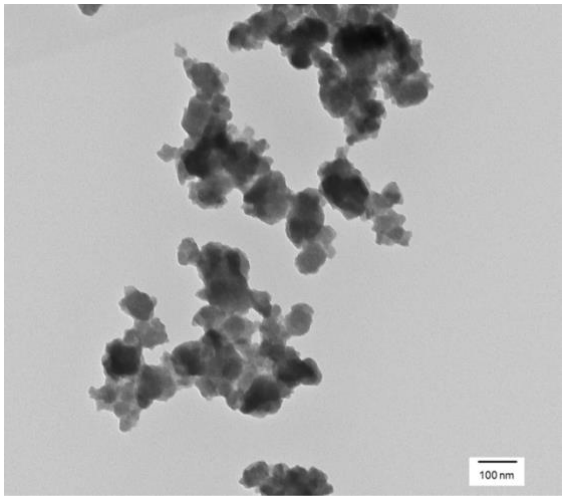

Figure 5-2 TEM image of co-precipitated ^{89}Zr-nHAp

The stability of the co-precipitated ^{89}Zr-nHAp over the course of 7 days (~ 2 half-lives) showed that 96 ± 3% of the radioactivity remained associated with the particles. This stability showed no significant difference compared to the previous work where the ^{89}Zr labeled sphere-shaped particles were 100 ± 3% ($p = 0.105$) and ^{89}Zr labeled needle-shaped particles were 98.2 ± 1.2% ($p = 0.425$) intact after two half-lives. The particle size in conjunction with the stability results led to the decision to use the co-precipitated ^{89}Zr-nHAp particles for further experiments involving the modification of the nanoparticle for receptor targeting.

Modification of ^{89}Zr-nHAp with phospha-TOC

The QTOF calibration curve for phospha-TOC and washes for the modified ^{89}Zr-nHAp-phospha-TOC are provided in Figure 5-3. The QTOF data showed that there was no phospha-TOC present after the fifth wash therefore validating that the mass peak at 1129 on the final product is the phospha-TOC attached to the ^{89}Zr-nHAp. The final amount of the phospha-TOC attached to the nHAp was 1.019 µmol/mg of nHAp.

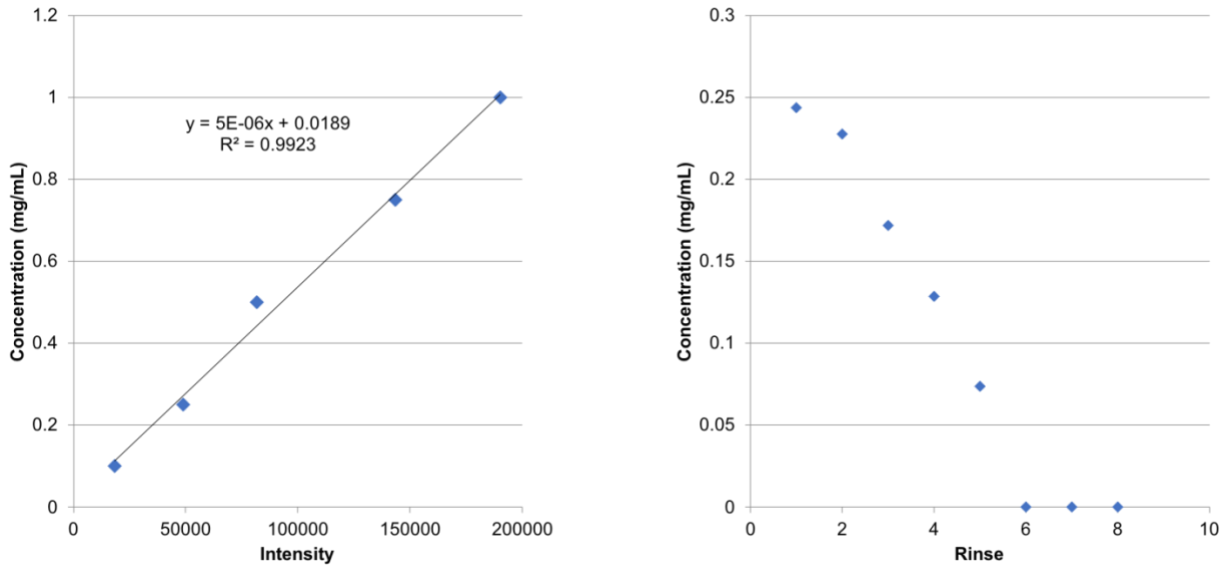

Figure 5-3 Phospha-TOC concentration calibration curve (left)
and the phospha-TOC measurement for each wash (right)

Cell Studies with ^{89}Zr-nHAp-phosph-TOC

Figure 5-4 shows the percent binding of the ^{89}Zr-nHAp-phospha-TOC per µg of protein where non-blocking had 0.012 ± 0.002 %/µg, blocking had 0.0088 ± 0.0013 %/µg and bare particles had 0.0013 ± 0.0002 %/µg, and the percent binding of the ^{89}Zr-nHAp-phospha-TOC per million cells where non-blocking yielded 2.3 ± 0.7 % per million cells, blocking yielded 1.5 ± 0.3 % per million cells and bare particles yielded 0.18 ± 0.03 % per million cells. In both graphs, the data show there is significant difference between the non-blocked cells and the blocked cell for both per µg of protein (p= 0.0006) and for the percent binding per million of cells (p=0.0007). This is also true of the comparison between the non-blocked cells targeted with ^{89}Zr-nHAp-phospha-TOC and the cells that were targeted with bare particles (no peptide), where the p-value for the percent binding per µg of protein was 0.0009 and for the percent binding per millions of cells was 0.0006. This study shows that the bare particles have minimal nonspecific binding and the

success of the nHAp modification for targeting the SSTR2 receptors. These cell studies confirm that the ^{89}Zr-nHAp is modified with phospha-TOC and illustrates specific targeting.

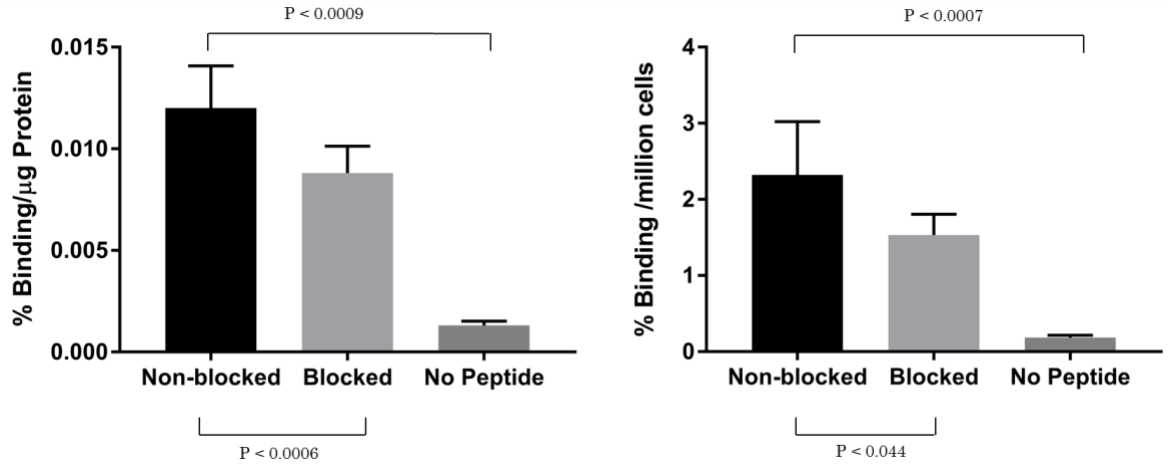

Figure 5-4 Cell Study using AR42J cell which overexpress SSTR2 receptors

Animal Studies with ^{89}Zr-nHAp-phospha-TOC

PET imaging studies for the non-blocking mice at 4, 24, and 72 hours with the post-imaging biodistribution data can be found in figure 5-5. The images show tumor uptake at each time point. The standard uptake value (SUV) data shown in Table 5-1 shows the highest SUV at 24 hours where the SUV for 4 h, 24 h and 72 h was 0.34 ± 0.19, 0.9 ± 0.5, and 0.6 ± 0.2, respectively, although there is no significant difference between the three points (p=0.1073). Furthermore, in Table 5-1, there is no significant difference in SUV between the tumor and the background (muscle) at 4 h. However, a significant difference was found between the tumor and the background (muscle) during the 24-hour and 72-hour time periods with p-values of 0.026 and 0.0055, respectively. The biodistribution shows no significant difference between tumor uptake for each time point (p = 0.97) with background levels observed in the lungs, spleen, and liver.

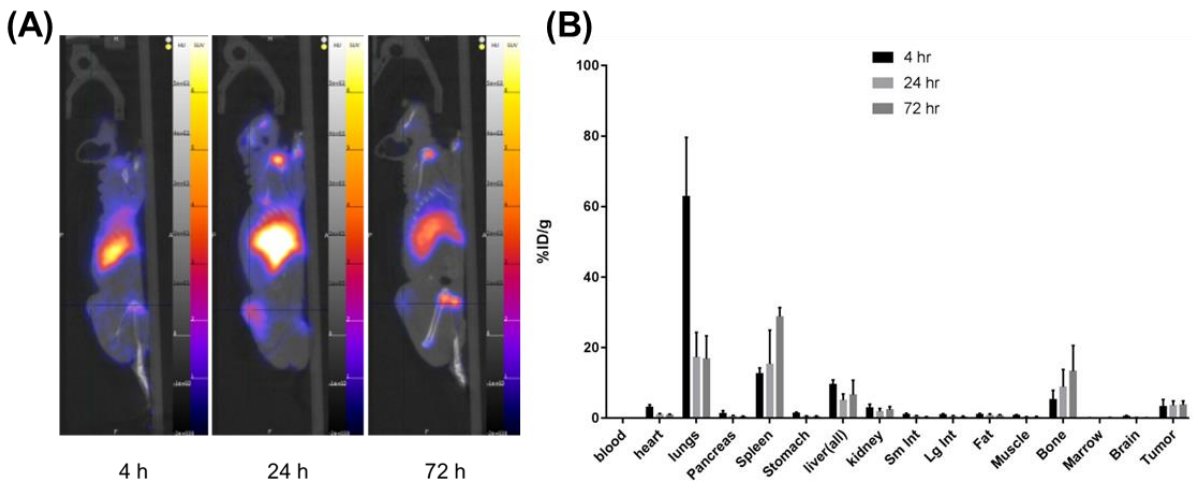

Figure 5-5 (A) PET imaging at 4, 24, and 72 hours of ^{89}Zr-nHAp-phospha-TOC targeting agent for SSTR2 receptors and (B) the corresponding post-imaging biodistribution

Table 5-1 SUV data for the different imaging time points for tumor and muscle

Time Point	SUV for Tumor	SUV for Muscle	Tumor to Muscle comparison p-value
4 hours	0.34 ± 0.19	0.26 ± 0.08	0.24
24 hours	0.9 ± 0.5	0.24 ± 0.05	0.026
72 hours	0.6 ± 0.2	0.165 ± 0.017	0.0055
24 hours Blocked	0.16 ± 0.09	0.09 ± 0.02	0.079

Blocking studies were conducted with post imaging biodistribution conducted at 24 hours post injection. Figure 5-6 displays the results of the blocking study compared to the non-blocking study at the 24-hour time point. Image analysis illustrated a significant difference in the SUV found in the non-blocked tumor relative to the blocked tumor at 24 h post injection. The SUV value data for the non-blocked vs the blocked tumor was 0.9 ± 0.5 and 0.16 ± 0.09 with a p-value of 0.018. In the biodistribution, significantly less uptake was found in the blocked tumor than

the non-blocked tumor (p-value 0.042). For all other organs there was no significant difference in uptake (p-values > 0.05). Overall, the blocking study illustrated specific targeting of the ^{89}Zr-nHAp-phospha-TOC to the SSTR2 receptors in this tumor model.

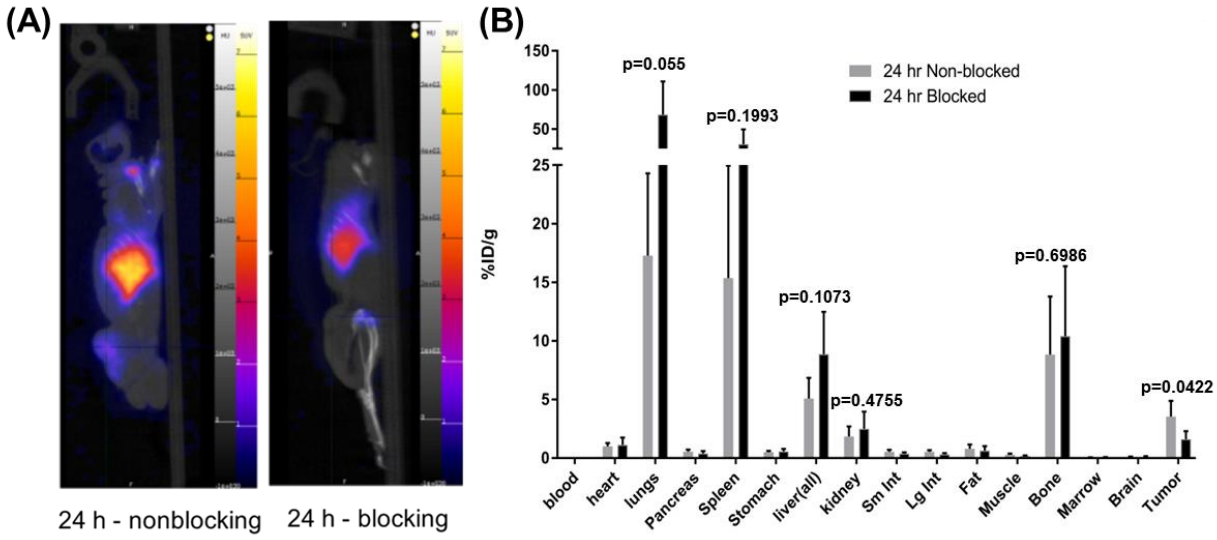

Figure 5-6 PET imaging at 24 hours of ^{89}Zr-nHAp-phospha-TOC for non-blocking versus block of SSTR2 receptors using TOC and the corresponding post-imaging biodistribution

5.4 Conclusion

Our work shows that the co-precipitated ^{89}Zr-nHAp had similar stability with better particle size distribution compared to the commercially available nHAp in our previous work (Chapter 4). The ^{89}Zr-nHAp was modified with phospha-TOC and the modified nHAp showed specific targeting to SSTR2 on the AR42J cell line. The preliminary animal studies further confirm the specific targeting between the non-blocked and blocked animal model. Overall, the preliminary studies with ^{89}Zr-nHAp-phospha-TOC are very promising for nHAp as a new platform for PET imaging agents.

5.5 Acknowledgments

The authors of this article would like to thank the Department of Radiology at the University of Alabama at Birmingham (UAB) for funding, the UAB Cyclotron Facility for the production of ^{89}Zr and the UAB Small Animal Imaging Facility for PET imaging and biodistribution studies. The UAB Small Animal Imaging Facility is supported through the UAB Comprehensive Cancer Center P30CA013148 grant from NIH.

5.6 References

1. Hoshyar, N.; Gray, S.; Han, H.; Bao, G., The effect of nanoparticle size on in vivo pharmacokinetics and cellular interaction. *Nanomedicine (Lond)* **2016,** *11* (6), 673-92.
2. Salata, O., Applications of nanoparticles in biology and medicine. *J Nanobiotechnology* **2004,** *2* (1), 3.
3. McNamara, K., Nanoparticles in biomedical applications. *Advances in Physics* **2017,** *2* (1), 54-88.
4. Queern, S. L.; Aweda, T. A.; Massicano, A. V. F.; Clanton, N. A.; El Sayed, R.; Sader, J. A.; Zyuzin, A.; Lapi, S. E., Production of (89)Zr using sputtered yttrium coin targets *Nucl Med Biol* **2017,** *50*, 11-16.
5. Holland, J. P.; Sheh, Y.; Lewis, J. S., Standardized methods for the production of high specific-activity zirconium-89. *Nucl Med Biol* **2009,** *36* (7), 729-39.
6. Van Dongen, G. A. M. S.; Visser, G. W. M.; Lub-de Hooge, M. N.; de Vries, E. G.; Perk, L. R., Immuno-PET: A navigator in monoclonal antibody development and applications. *Oncologist* **2007,** *12*, 1379-89.
7. Deri, M. A.; Zeglis, B. M.; Francesconi, L. C.; Lewis, J. S., PET imaging with ^{89}Zr: from radiochemistry to the clinic. *Nucl Med Biol* **2013,** *40* (1), 3-14.
8. Abou, D. S.; Ku, T.; Smith-Jones, P. M., In vivo biodistribution and accumulation of (89)Zr in mice. *Nucl Med Biol* **2011,** *38* (5), 675-81.
9. Zhou, H.; Lee, J., Nanoscale hydroxyapatite particles for bone tissue engineering. *Acta Biomater* **2011,** *7* (7), 2769-81.
10. Kojima, C.; Watanabe, K., Adsorption and desorption of bioactive proteins on hydroxyapatite for protein delivery systems. *J Drug Deliv* **2012,** *2012*, 932461.
11. Matsumoto, T.; Okazaki, M.; Inoue, M.; Hamada, Y.; Taira, M.; Takahashi, J., Crystallinity and solubility characteristics of hydroxyapatite adsorbed amino acid. *Biomaterials* **2002,** *23* (10), 2241-7.
12. Radford, L.; Gallazzi, F.; Watkinson, L.; Carmack, T.; Berendzen, A.; Lewis, M. R.; Jurisson, S. S.; Papagiannopoulou, D.; Hennkens, H. M., Synthesis and evaluation of a (99m)Tc tricarbonyl-labeled somatostatin receptor-targeting antagonist peptide for imaging of neuroendocrine tumors. *Nucl Med Biol* **2017,** *47*, 4-9.

13. Storch, D.; Behe, M.; Walter, M. A.; Chen, J.; Powell, P.; Mikolajczak, R.; Macke, H. R., Evaluation of [99mTc/EDDA/HYNIC0]octreotide derivatives compared with [111In-DOTA0,Tyr3, Thr8]octreotide and [111In-DTPA0]octreotide: does tumor or pancreas uptake correlate with the rate of internalization? *J Nucl Med* **2005,** *46* (9), 1561-9.
14. Ghosh, S. C.; Hernandez Vargas, S.; Rodriguez, M.; Kossatz, S.; Voss, J.; Carmon, K. S.; Reiner, T.; Schonbrunn, A.; Azhdarinia, A., Synthesis of a Fluorescently Labeled (68)Ga-DOTA-TOC Analog for Somatostatin Receptor Targeting. *ACS Med Chem Lett* **2017,** *8* (7), 720-725.
15. Ashokan, A.; Gowd, G. S.; Somasundaram, V. H.; Bhupathi, A.; Peethambaran, R.; Unni, A. K.; Palaniswamy, S.; Nair, S. V.; Koyakutty, M., Multifunctional calcium phosphate nano-contrast agent for combined nuclear, magnetic and near-infrared in vivo imaging. *Biomaterials* **2013,** *34* (29), 7143-57.
16. Moller, L. N.; Stidsen, C. E.; Hartmann, B.; Holst, J. J., Somatostatin receptors. *Biochim Biophys Acta* **2003,** *1616* (1), 1-84.

Chapter 6

Conclusions & Future Work

6.1 Conclusions

Positron emission tomography (PET) imaging is a non-invasive and highly quantitative way to diagnosis different diseases in several medical fields including oncology, neurology and cardiology. The idea of personalized care using PET imaging is a key driver for advancing research into developing new platforms for PET imaging agents leading to more effective diagnosis and better treatment planning. ^{89}Zr has a long half-life, a low maximum positron energy and established radiochemistry that has raised the demand for this isotope in nuclear medicine. Although ^{89}Zr has great potential as PET nuclide, it is a known bone seeker meaning if it decomplexes it will be taken up in the bone. This bone uptake can be exploited by using the natural affinity of ^{89}Zr to create for nHAp based PET agents. Overall this work provides the basis (proof of concept) for showing the implementation of nHAp as a new platform of PET imaging agents.

^{89}Zr Production and Separation

Our initial studies aimed to produce ^{89}Zr on the UAB TR-24 cyclotron. The proton beam energy was degraded using an aluminum degrader to prevent the production of ^{88}Zr and an yttrium sputtered target was designed to be compatible with the existing coin slot holder. The control over the yttrium mass and the target cross section area allowed for an efficient separation of the ^{89}Zr from the yttrium with a final product with reasonable specific activity. This method is now the standard practice for the production of ^{89}Zr at UAB for human and research use.

An alternative method of separation for ^{89}Zr was investigated in collaboration with Brookhaven National Laboratory, to allow for ease in automating the separation system and potentially

eliminating the need to remove the chelator before injection. Low-level activity separations of ^{89}Zr from Y on pCST resin using IDA to elute off the ^{89}Zr showed reproducibility with successful test labeling of a DFO conjugated antibody. These results show the potential for this alternative method of separation.

Development of nHAp as PET Tracer

The natural affinity of ^{89}Zr and other radionuclides for bone was exploited to synthesize radiolabeled nHAp particles and develop rapid radiochemistry to enable a new class of imaging agents with kit-like formulations. The ^{89}Zr-nHAp was shown to be a good candidate for the development of new targeted PET imaging agents while ^{153}Sm-nHAp was shown to be a strong candidate for therapy. The particles were easily labeled with bone seeking radionuclides and have high in vitro stability with little bone uptake in vivo.

A rapid modification method for nHAp using an analog of the peptide TOC to target SSTR2 receptors was developed using the preparation of co-precipitated ^{89}Zr nHAp. The co-precipitated ^{89}Zr-nHAp had similar stability with better particle size distribution compared to the commercially obtained sphere-shaped and needle-shaped nHAp. The ^{89}Zr-nHAp was rapidly modified with phospha-TOC and the resulting agent showed specific targeting for the SSTR2 receptors. The preliminary animal studies further confirm the specific targeting between the non-blocked and blocked animal model. Overall, the preliminary studies with ^{89}Zr-nHAp-phospha-TOC are very promising for nHAp as a new platform for PET imaging agents.

6.2 Future Work

While the low-level activity separations with our new method of ^{89}Zr purification were promising, full size production scale separations should be performed. The production scale separations will allow for comparisons of large batch specific activities and test labeling comparisons. Further ICP-MS analysis should be conducted on the production scale separation fractions for both Y and Ti. ICP-MS of the Ti will supply information on the stability of the resin as more radioactivity is added to the column.

While the preliminary animal studies of the ^{89}Zr-nHAp-phospha-TOC were promising, further studies should be conducted for reproducibility. Further investigations should be carried out to determine if the bone uptake in the preliminary studies can be contributed to the ^{89}Zr decomplexing or nHAp adhering to the bone. Since nHAp is used in bone grafts, it might have an affinity for damaged or growing bone. This may be investigated using aged normal mice that have been tested negative for bone disease. There is also a huge potential for other studies using the co-precipitation method to form nHAp as a multilabeled agent for theragnostic applications. As example, multilabeling co-precipitated nHAp with ^{89}Zr and ^{153}Sm would allow for PET imaging with the ^{89}Zr while therapy is occurring using ^{153}Sm.

In conclusion, the work present in this thesis has set up excellent groundwork for the development of nHAp as a new platform for PET imaging agents. This work has shown the rapid labeling and modification for the development of targeted agents is possible for nHAp. The implementation of bone seeking radionuclides in the co-precipitation method of nHAp opens new avenues of research for applications in imaging and targeted therapy.